

The Motion of Stars and the Accretion of Matter in
the Fermion Ball and Black Hole Scenarios of the
Galactic Centre

Samuel James Alexander Halliday

July, 2002

Abstract

The motion of stars S0-1, S0-2 and S0-4, in the vicinity of the galactic centre, is investigated using a χ^2 analysis of the parameters in our line of sight. The resulting phase spaces for the black hole and fermion ball scenarios are compared. We find that due to the lack of accurate z or v_z data, the upper limit of required observational time to discriminate between the scenarios is of the order 30 to 40 years. Such z and v_z data might allow us to eliminate one of the scenarios immediately.

The spectrum from the Sgr A* region is also investigated using a *simple* Newtonian, optically thick and geometrically thin model for each scenario. As has already been known for some time, this technique is not applicable to a possible black hole scenario at Sgr A* and as a consequence, is incapable of explaining a cut-off in the spectrum at around 10^{13}Hz . This cut-off follows naturally from the fermion ball potential distribution in this simple model. It should be noted that Advection Dominated Accretion Flow models (not investigated here) are able to predict the observed spectrum for the black hole scenario.

Contents

1	Introduction	1
1.1	The Sgr A Complex	1
1.2	Alternatives to the Black Hole Scenario	1
1.3	Fermion Candidates	5
1.4	Where do the Fermions Come From?	6
1.5	Thesis Objectives	7
2	Non-Relativistic Mass Distribution	8
2.1	Lan�-Emden Equation	9
2.1.1	Thomas-Fermi	11
2.2	Limits on Fermion Mass	11
3	Relativistic Mass Distribution	14
3.1	Hydrostatic Equilibrium	14
3.1.1	Exterior Solution (Schwarzschild)	15
3.1.2	Interior Solution (Oppenheimer and Volkoff)	16
3.2	Equation of State for a Relativistic Degenerate Fermi Gas	16
3.3	Mass Distribution	18
4	Formation of a Fermion Ball	21
4.1	Analogy to a Boson Star	21
4.2	Time Evolution of the Collapse	22
5	Dynamics of Stars near the Galactic Centre	24
5.1	Closed and Precessing Orbits	24
5.2	Newtonian Motion	25
5.3	χ^2 Reduction of z and v_z	26
5.3.1	Notes on χ^2	26
5.3.2	Best Fits	27
5.4	Analysis	31
5.5	The Importance of v_z and z	39
6	Spectrum by Accretion of Matter	42
6.1	Source of the Accreting Gas	42
6.2	Viscous Torque as a Means of Energy Release	44
6.3	The Accretion Process	45
6.3.1	Dissipation Rate for a Black Hole	46
6.3.2	Dissipation Rate for a Fermion Ball	47
6.4	Temperature Distribution Due to Accretion	48
6.4.1	Black Hole	48
6.4.2	Fermion Ball	48
6.5	A Toy Model	49
6.5.1	The Optically Thick Approximation	49

6.6	Accretion Spectrum	49
6.6.1	The Radio and Microwave Spectrum	50
6.6.2	Star Birth	52
7	Fermion Halo and Dark Matter in the Galaxy	53
7.1	Dark Matter Within Our Galaxy	53
7.2	The Fermion Halo	55
7.3	Rotation Curve of Our Galaxy	56
8	Conclusions	58
A	Reduction of Terms in 6.4.2	59
B	Radiation Processes	60
C	Numerical Techniques	62

1 Introduction

Black holes are where God divided by zero
– Anonymous et al.

It is well accepted that the centres of many galaxies harbour a super-massive compact dark object [1]. The masses of roughly 20 such objects, located in inactive galaxies, have been established to lie in the range between $10^6 \rightarrow 3 \times 10^9 M_\odot$ [2]. The radii of these objects are less well determined. Studies of the variability of the luminosities of active galactic nuclei place upper limits on their radii of a few 10^{-2} pc [1].

1.1 The Sgr A Complex

In the case of the nearest super-massive compact dark object at the centre of the Milky Way, one can, based on the statistics of proper motion of the stars in the central cluster, conclude that a dark mass of $\sim 2.6 \times 10^6 M_\odot$ must be within 0.015 pc from the dynamical centre of the galaxy [3].

The central region of our own galaxy is Sgr A (Figure 1). It consists of three main parts, Sgr A West (Figure 2), Sgr A East (Figure 3) and a very strong radio source known as Sgr A*, believed by many to be a black hole. The proper motion of Sgr A* has been established to be smaller than 20 km/s [4]. In order to maintain this small velocity for an extended period of time, the mass of Sgr A* needs to be larger than $10^3 M_\odot$. Moreover, Very Large Baseline Array (VLBA) measurements indicate that the radio emission takes place within a region of a few AU [5].

Sgr A* has been extensively studied at various wavelengths. The X-ray region (Figure 4) is of great importance as it reveals an interesting ‘flaring’ of the spectrum. A compilation of spectral data is presented in Figure 5. The infra-red (IR), optical and ultraviolet (UV) regions are devoid of detected emission. In the optical and UV regions, this is solely due to the enormous amount of Galactic foreground extinction.

1.2 Alternatives to the Black Hole Scenario

It is natural to speculate that the objects observed in other galaxies are the same as the object at our own galactic centre. The most commonly accepted idea is that Sgr A* is a black hole. The formation of such super-massive black holes prior to the onset of the quasar era ($z \approx 6$) still remains a mystery. Thus until an event horizon is actually observed, it is important to study alternative scenarios.

Most of the alternative scenarios to the black hole paradigm of Sgr A* usually concentrate either on predictions of the spectrum, or dynamics of the cluster stars. Some of these ideas and their associated problems are briefly discussed.

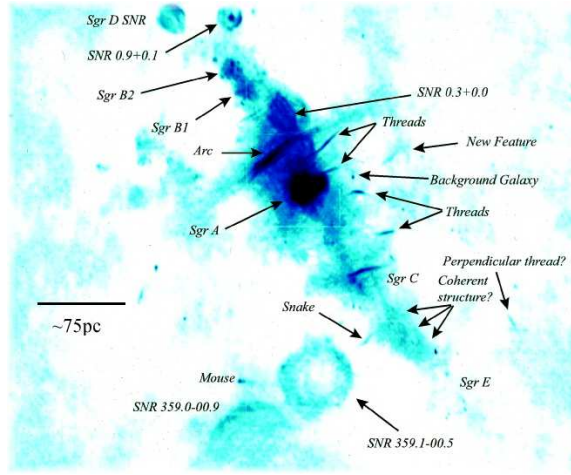


Figure 1: Wide field radio image of the central region of the Milky Way, performed at $\lambda=90\text{cm}$ [7].

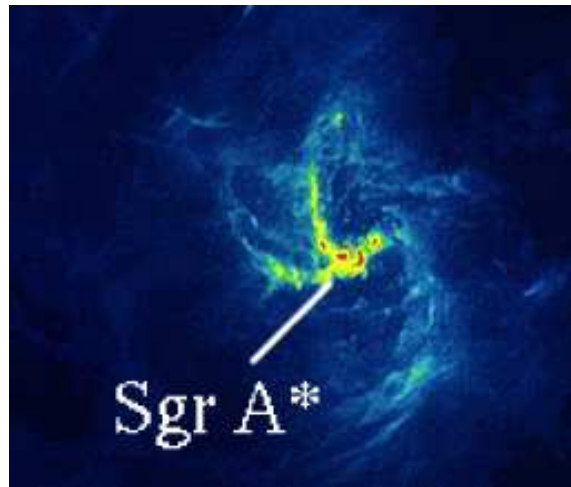


Figure 2: $\lambda=6\text{cm}$ image of Sgr A. Close to Sgr A* lies a collection of filamentary structures known as Sgr A West. The emission from Sgr A West is due to ionised gas that is heated by the numerous young, hot stars in the region. (Image courtesy of Prof. K. Y. Lo, University of Illinois).

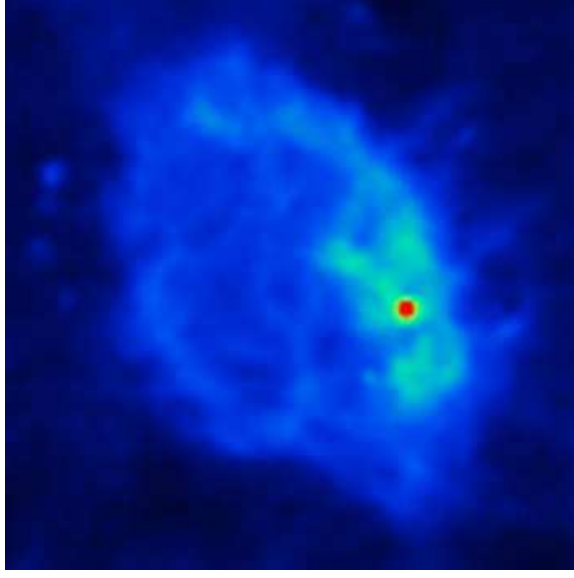


Figure 3: $\lambda=20\text{cm}$ image of Sgr A. The light blue, shell-like feature (Sgr A East) is thought to be a supernova remnant. The red point in the image is the Sgr A* radio source (Image courtesy of R. Plante, University of Illinois).

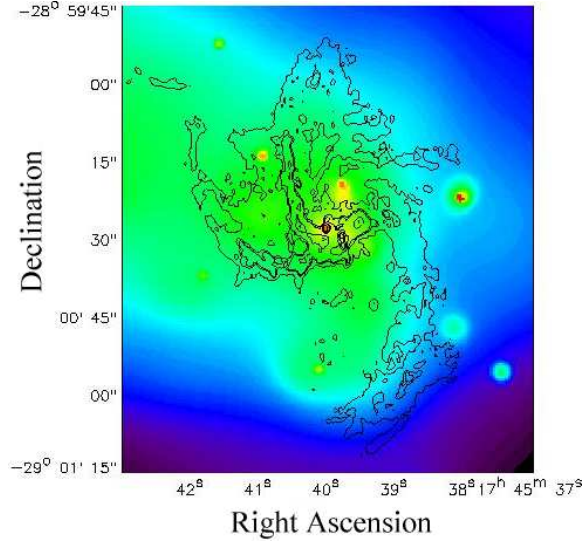


Figure 4: $0.5 \rightarrow 7\text{keV}$ image of the central region of the Milky Way. The image has been adaptively smoothed and flat-fielded. Overlaid on the image are $\lambda=6\text{cm}$ contours from Figure 2. X-ray emission from the vicinity of Sgr A* appears as a red dot at $17^{\text{h}}45^{\text{m}}40.0^{\text{s}}$, $-29^{\circ}00'28''$ (J2000.0) [8].

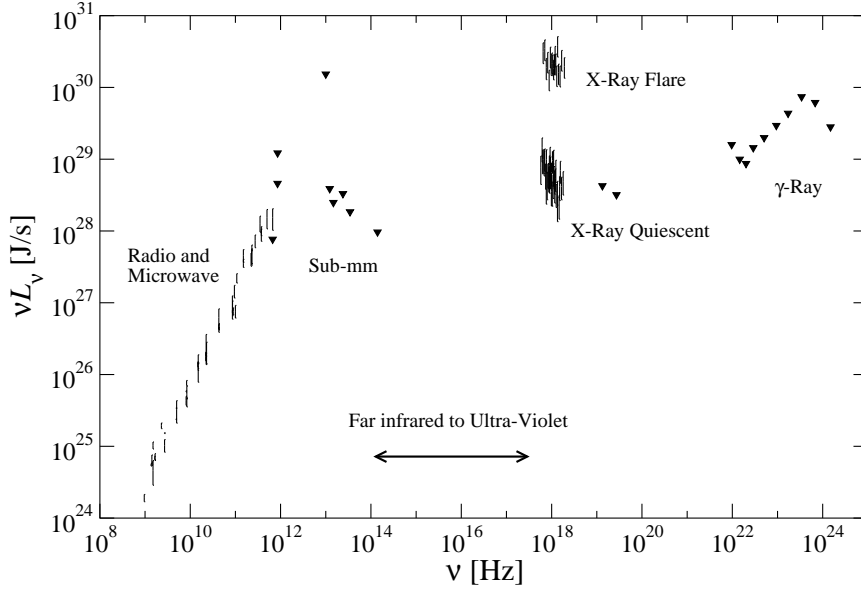


Figure 5: Compilation of spectral data in the direction of Sgr A. Triangular data points are upper limits [52].

One idea that has already been explored is that of a super-massive star consisting of normal matter, with an even heavier accretion disk [6]. This scenario meets problems in explaining the IR spectrum. A compact and dark stellar cluster has also been proposed as a solution [9]. Such a cluster requires evaporation and collision time-scales larger than the lifetime of our galaxy. This is more likely to be fulfilled using a cluster of sub-stellar objects. Some alternatives have even touched upon the bizarre, such as the claim of a ‘white hole’ at our galactic centre [10].

An interesting theory uses neutralinos to explain dark matter evolution and distribution in the galaxy [22]. The neutralino is postulated as the main component of dark matter. The neutralino is the lightest SuSy particle, a superposition of the photino, zino and the super-partners of the neutral scalar Higgs particles.

$$\chi = N_1 \tilde{\gamma} + N_2 \tilde{Z}^0 + N_3 \tilde{H}_1^0 + N_4 \tilde{H}_2^0$$

It is stable due to R-parity conservation, and should have a mass $\sim 100\text{GeV}$. This theory predicts a non-dissipative gravitational singularity or ‘spike’ at the centre of our galaxy, but this has not been observed. The annihilation processes would result in a distinctive γ -ray and radio spectrum. As the γ -ray maps of the galactic centre are somewhat incomplete and of low resolution, and also due to the shear scale of this theory, much more investigation (far beyond the scope of the galactic centre) is required in order to test it fully.

In a ‘from scratch’ approach to postulating the form of a super-massive compact dark object, it is vital to look at the object’s composition. It is natural, considering the incredible masses involved, to postulate that the objects are made from the most fundamental of stable particles, as opposed to some exotic blend. The particle world consists of bosons and fermions. If we consider a single ingredient particle then the super-massive objects will be either bosonic or fermionic.

A self-gravitating, degenerate, ‘fermion ball’ has already been proposed [11, 12, 13, 14, 15, 16]. As the constituent particles are all fermions, Pauli’s Exclusion Principle dictates that the particles exert a degeneracy pressure upon each other, which counteracts the gravitational force. In contrast to the proposed fermion ball, a ‘boson star’ has also been presented in [17], the Heisenberg uncertainty principle keeping the system from collapsing into a black hole. However such boson stars are limited in maximal mass by a $M \sim R^{-1}$ relation as opposed to $M \sim R^{-3}$ for a fermion ball (in a non-relativistic approach). It is therefore impossible for the boson stars to explain the most massive objects in galactic centres (such as M87 in the Virgo cluster [1]) as well as the least massive such as Sgr A*. A fermion ball is capable of explaining both the most and least massive of the objects through 16keV fermions.

1.3 Fermion Candidates

Although this thesis will treat the fermion ball as consisting of an undetected neutral, massive fermion, it is worthwhile to comment on possible candidates for such a particle. If such a particle does not exist, then the fermion ball scenario is obviously an impossible one. We will see later that we require a fermion of mass $\sim 16\text{keV}$, and this will be the main factor in discriminating candidates. It is therefore clear that the neutralino is not a viable candidate as it has a predicted mass in the GeV range.

The most obvious neutral fermion is the neutron. However, it has a mass of 940MeV, which is much too high for our requirements.

Neutrino stars, have been postulated as far back as 1964 [18], in order to explain quasars. Unfortunately, the mass of active neutrinos are too small to be candidates for the galactic fermion ball. Present upper limits are $\leq 2.2\text{eV}$ for each of the 3 light species [19, 20]. Only 3 active neutrinos can exist on account of limits on the invisible decay width of the Z^0 boson [21]. It has also been shown that if the dark matter in the universe were comprised of neutrinos of mass $\sim 16\text{keV}$, it would over-close the universe by orders of magnitude [23]. However, a possible candidate could be a sterile neutrino, which does not participate in weak interactions but is mixed with at least

one active neutrino. For two-neutrino mixing

$$\begin{aligned} |\nu_\alpha\rangle &= \cos\theta|\nu_1\rangle + \sin\theta|\nu_2\rangle \\ |\nu_s\rangle &= -\sin\theta|\nu_1\rangle + \cos\theta|\nu_2\rangle \end{aligned} \tag{1}$$

where $|\nu_\alpha\rangle$ and $|\nu_s\rangle$ are active ($\alpha = e, \mu, \tau$) and sterile neutrino flavour eigenstates, respectively. $|\nu_1\rangle$ and $|\nu_2\rangle$ are the mass eigenstates with mass eigenvalues m_1 and m_2 respectively. Such mixing renders these species not truly sterile and as a result, they can decay. We require this decay time to be large and therefore the mixing angle to be small. Sterile neutrinos have been suggested as a candidate for hot, warm or cold dark matter [24, 25], with a predicted mass range 1keV→10MeV due to suspicions of multiple generations.

Alternatively the fermion may be either the gravitino, postulated in super-gravity theories with a mass range of 1keV→100GeV [26] or the axino with a predicted mass 1keV→1GeV, as predicted by the super-symmetric extensions of the Peccei-Quinn solution to the strong CP problem [27, 28, 29].

1.4 Where do the Fermions Come From?

It is also important to understand how such a large gathering of fermions could originate.

If we assume a small primordial lepton asymmetry, sterile neutrinos would have been produced non-resonantly at the beginnings of the universe. Early constraints on production were derived in [30, 31]. Analytic estimates were later made on relic sterile neutrino abundance [32]. Active neutrinos are still produced today, mainly within the nuclear reactions of stars and from natural neutron decay. These active neutrinos could resonate into the sterile state, as previously mentioned, and therefore yield an additional source of sterile neutrino. This again however, depends upon the (as yet unknown) decay time of the sterile neutrino.

Gravitinos are created in the early universe with a cosmologically significant abundance. They could be created either thermally after reheating [33], or non-thermally from the vacuum fluctuations, before horizon exit during inflation [34].

The axino is a super-symmetric prediction, it can therefore arise from the moment when low energy super-symmetry is softly broken. Production can be either thermal or non-thermal. Axinos have a predicted lifetime of the order $> 10^{40}$ years.

Our three candidates are primordially produced in the early universe, and (assuming long lifetimes) are therefore all acceptable candidates for at least part of the missing dark matter. This thesis will not focus upon the dark matter implications of the required fermions. However, remarks will be made about effects that an associated fermion halo may have on our own galaxy's rotation curve problem.

1.5 Thesis Objectives

Prediction is very difficult, especially of the future.
– Niels Bohr

We start by introducing a formalism for describing the potential and mass distribution within a fermion ball, using Newtonian mechanics. This will later be extended to a relativistic approach. After discussing the formation theory, this potential will be used to predict the motions of stars moving within the fermion ball. Comparison will be made with black hole predictions and experimental observations. We present the data in the form of high resolution χ^2 phase space plots for the unknown position and velocity parameters in our line of sight.

A simple non-relativistic accretion ‘toy model’ will be developed for each scenario to derive the observed spectrum from Sgr A.

Finally, we remark upon the ability of the fermion halo theory to explain the dark matter distribution within our galaxy.

2 Non-Relativistic Mass Distribution

*I know that this defies the law of gravity,
but, you see, I never studied law.
– Bugs Bunny*

In order to obtain the mass distribution of the fermion ball, let us first look at a simple Newtonian model [16], in which the gravitational potential satisfies Poisson's equation

$$\nabla\Phi(r) = -4\pi G\rho_\nu(r) \quad (2)$$

where G is Newton's gravitational constant and $\rho_\nu(r)$ the mass density of the fermions and anti-fermions at a particular radius r . The self-gravity of the fermionic matter may be balanced with its degeneracy pressure, obeying the equation of hydrostatic equilibrium

$$\frac{1}{\rho_\nu} \frac{dP_\nu}{dr} + \frac{d\Phi}{dr} = 0 \quad (3)$$

Here the pressure is given by the polytropic equation of state for non-relativistic fermionic matter at zero temperature.

$$P_\nu = K\rho_\nu^{\frac{5}{3}} \quad (4)$$

with the constant K given by [14]

$$K = \left(\frac{6}{g_\nu}\right)^{\frac{2}{3}} \frac{\pi^{\frac{4}{3}} \hbar^2}{5m_\nu^{\frac{8}{3}}} \quad (5)$$

where g_ν represents the number of degrees of freedom of the fermions (spin and particle-antiparticle degeneracy), either 2 (Majorana) or 4 (Dirac), m_ν being the fermion rest mass. We thus obtain

$$\frac{5}{2}K\rho^{\frac{2}{3}} + \Phi = E_0 \quad (6)$$

with E_0 as the potential at the outer radius (R_0). Taking the fermion ball to be spherically symmetric (and hence the gravitational potential), it follows from (2) that

$$\frac{1}{r} \frac{d^2(r\Phi)}{dr^2} = -4\pi G\rho_\nu(r) \quad (7)$$

and using the substitution

$$f = E_0 - \Phi = \frac{5}{2}K\rho^{\frac{2}{3}} \quad (8)$$

the Poisson equation may be re-written as

$$\frac{1}{r} \frac{d^2(rf)}{dr^2} = -4\pi G \left(\frac{2f}{5K} \right)^{\frac{3}{2}} \quad (9)$$

By defining $u = rf$, (9) is more easily solved. It is now more convenient to work in the dimensionless units as given by

$$v = \frac{u}{GM_\odot} \quad (10)$$

$$x = \frac{r}{a_\nu} \quad (11)$$

with

$$a_\nu = \frac{5K}{2GM_\odot^{\frac{1}{3}}(4\pi)^{\frac{2}{3}}} \quad (12)$$

2.1 Lané-Emden Equation

The previous substitutions reduce (9) to the Lané-Emden equation

$$\frac{d^2v(x)}{dx^2} = -\frac{v(x)^{\frac{3}{2}}}{x^{\frac{1}{2}}} \quad (13)$$

which must be solved numerically. The boundary conditions are set such that u disappears at the outer radius R_0 (where the fermion density is zero) and the enclosed mass tends to M_B at the origin of the fermion ball. M_B is an arbitrary central baryonic mass, resident at the centre, allowing for the placement of a possible 'small' black hole or compact star cluster ($M_{\nu\bar{\nu}}$ the corresponding total fermionic mass). This implies

$$v(0) = \frac{M_B}{M_\odot} \quad v(x_0) = 0$$

The enclosed mass is found at any radius by integrating over the density

$$M(r) = \int_0^r 4\pi\rho_\nu(r)r^2dr \quad (14)$$

resulting for any dimensionless radius x as

$$M(x) = M_\odot [v(x) - xv'(x)] \quad (15)$$

and from (8), the gravitational potential is given as

$$\Phi(x) = \frac{GM_\odot}{a_\nu} \left[v'(x_0) - \frac{v(x)}{x} \right] \quad (16)$$

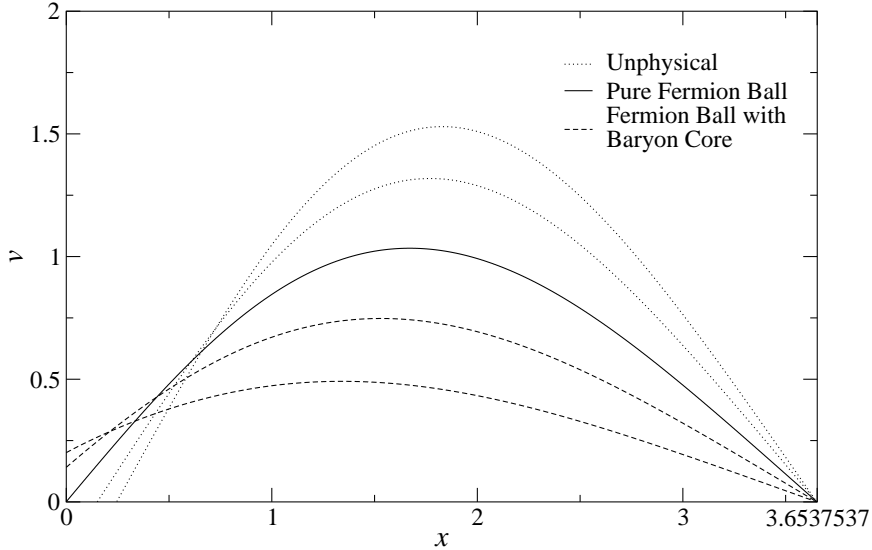


Figure 6: Solutions of the Lane-Emden equation

By the homology theorem, if $v(x)$ is a solution of the Lane-Emden equation, then

$$\tilde{v}(\tilde{x}) = A^3 v(Ax) \quad (17)$$

is also a solution, as long as A is a positive real number. This has several implications on the other quantities, and they must be scaled accordingly. Radii, enclosed mass and gravitational potential scale as

$$\tilde{R}_0 = \frac{R_0}{A} \quad \tilde{M}(\tilde{x}) = A^3 M(x) \quad \tilde{\Phi} = A^4 \Phi(x)$$

It is then sensible to solve the Lane-Emden equation only once and scale this to the required mass of the fermion ball. In the numerical solution, an initial value is required for v' , whether we choose to solve outward from the origin, or inward from the outer radius. This is initially set (arbitrarily) to unity, and by solving outward the endpoint value x_0 is obtained, allowing the equation to be solved inward with any $v'(x_0)$, corresponding to a central baryonic mass given by (before scaling)

$$\frac{dv(x_0)}{dx} = -\frac{M_B + M_\nu \bar{v}}{x_0 M_\odot} \quad (18)$$

Several solutions are shown in Figure 6. Using these solutions for $v(x)$ and $v'(x)$, it is now possible with the aid of (15) and (16) to calculate the mass distribution and potential within the fermion ball. Enclosed mass solutions are shown in Figure 7, potentials in Figure 8.

Although in these calculations we have allowed for a baryonic object at the centre, there is no direct evidence to suggest that this may be the

case. A baryonic object must have a very large mass in order to make a significant impact on the overall mass distribution, for this reason, all further calculations will assume that M_B is zero, and we therefore have a pure fermion ball.

2.1.1 Thomas-Fermi

The Newtonian mass distribution can also be described using the statistical method due to Thomas and Fermi [40], in which the local Fermi energy is set to the local gravitational binding energy [14]. The Lane-Emden equation (13) has much in common with the Thomas-Fermi equation, containing only an extra negation. The fermions are gravitationally attractive, opposed to electro-statically repulsive as in atomic physics where the Thomas-Fermi equation is applied. It is interesting to note that in 1928 Majorana found a semi-analytical solution to the Thomas-Fermi equation which remained unpublished until 2001 [41], unfortunately the method cannot be directly applied to the Lane-Emden equation.

2.2 Limits on Fermion Mass

Although these solutions are for 16keV fermions, solutions are easily obtainable for a variety of fermion masses. However, the overall fermion ball radius and mass is dependent upon the individual rest mass of the fermions and their degeneracy. As such, the minimal m_ν in order to constrain the ball fully within the boundaries of a total mass (M_T) and a maximal radius (R_0) is given by

$$m_\nu \geq \left(\frac{-3x_0^4 v'(x_0) \pi^2 \hbar^6}{64} \right)^{\frac{1}{8}} \left(\frac{1}{M_T R_0^3 g_\nu^2} \right)^{\frac{1}{8}} \quad (19)$$

Proper motion analysis [3] has imposed an enclosed mass of $2.6 \pm 0.2 \times 10^6 M_\odot$ at a radius of 0.015pc. Figure 9 displays several possible mass distributions corresponding to fermion rest masses. It is clear that when experimental errors are accounted for, the minimal allowed m_ν is approximately 16keV. For this reason, all calculations from here on in will be performed using 16keV fermions. This is based on the assumption that the fermion ball is fully constrained within the 0.015pc, a more massive fermion ball with fermions of lesser m_ν would still reproduce the results of [3], and this may be important later. It is also worth noting that the mass distribution for $g_\nu = 2$ fermions can easily be reproduced for $g_\nu = 4$ by slightly decreasing the rest mass according to

$$m_\nu g_\nu^{\frac{1}{4}} = \overline{m}_\nu \overline{g}_\nu^{\frac{1}{4}} \quad (20)$$

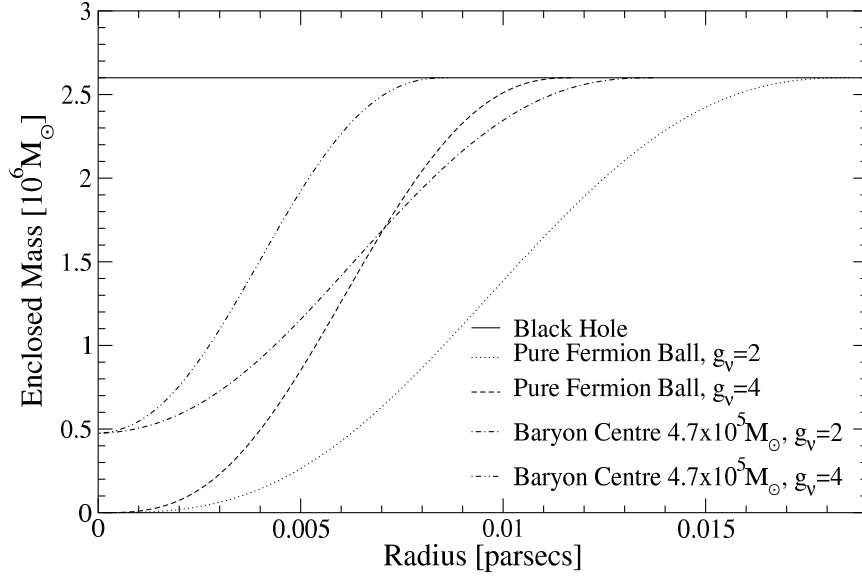


Figure 7: Enclosed mass distribution as a function of radius for 16keV fermions. The solid line denotes a black hole, which exhibits a constant enclosed mass at all radii.

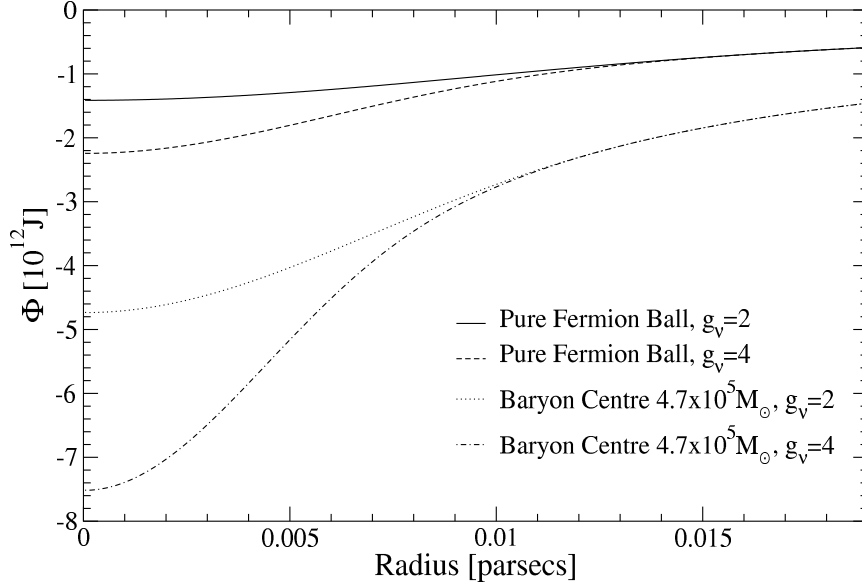


Figure 8: Gravitational potential as a function of radius for 16keV fermions.

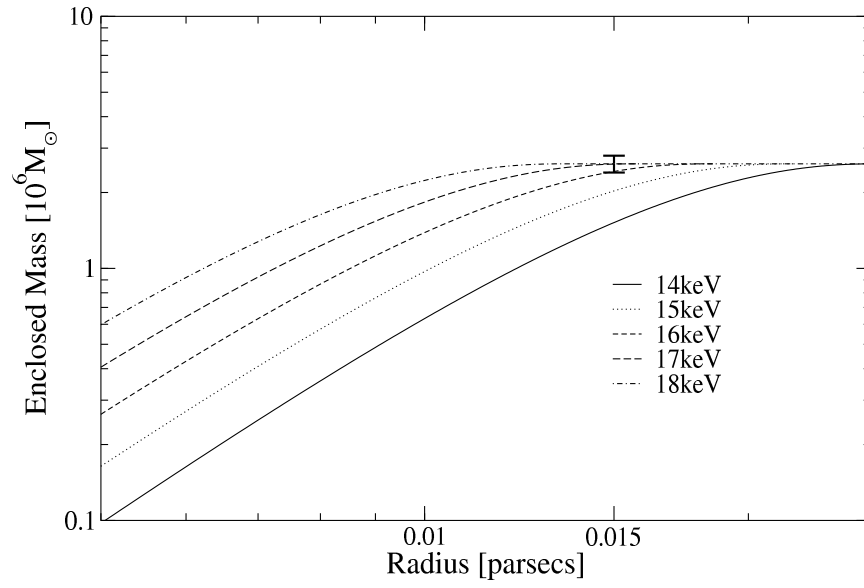


Figure 9: The enclosed mass as a function of radius for various fermion masses. Data point is from [3].

3 Relativistic Mass Distribution

*The probability of them visiting is directly proportional
to how much you feel like being left alone
– Einstein's Theory of Relatives*

In the previous section, a Newtonian description for the fermion ball mass distribution was outlined. When large masses are involved in calculations, it is often advisable to confirm the results with a relativistic treatment [15], and that is what this section will serve to provide. We choose to use units such that the speed of light and gravitational constant are unity ($c = G = 1$) and begin by assuming spherical symmetry of the fermion ball and a static solution, allowing the use of the Schwarzschild metric

$$ds^2 = e^{\nu(r)} dt^2 - e^{\lambda(r)} dr^2 - r^2 d\theta^2 - r^2 \sin^2 \theta d\phi^2 \quad (21)$$

Using Einstein's field equations we obtain

$$-8\pi T_{\mu\nu} = R_{\mu\nu} - \frac{1}{2} R g_{\mu\nu} + \Lambda g_{\mu\nu} \quad (22)$$

The solutions to the field equations [42] are

$$8\pi T_0^0 = e^{-\lambda} \left(\frac{\lambda'}{r} - \frac{1}{r^2} \right) + \frac{1}{r^2} - \Lambda \quad (23)$$

$$8\pi T_1^1 = -e^{-\lambda} \left(\frac{1}{r^2} - \frac{\nu'}{r} \right) + \frac{1}{r^2} - \Lambda \quad (24)$$

$$8\pi T_2^2 = 8\pi T_3^3 = \frac{e^{-\lambda}}{2} \left(\nu'' + \frac{\nu'^2}{2} + \frac{\nu'}{r} - \frac{\lambda'\nu'}{2} - \frac{\lambda'}{r} \right) \quad (25)$$

The approach to solving the relativistic mass distribution is to first solve the equation of hydrostatic equilibrium, interior and exterior to the fermion ball and then to introduce the relativistic equation of state for a Fermi gas.

3.1 Hydrostatic Equilibrium

The fermion ball is treated as a perfect fluid [43]

$$T^{\mu\nu} = \frac{\partial x^\mu}{\partial x_0^\alpha} \frac{\partial x^\nu}{\partial x_0^\beta} T_0^{\alpha\beta} \quad (26)$$

which by definition is incapable of exerting transverse stress. Therefore the quantities of proper mass density $\rho_0(r)$ and proper hydrostatic pressure $P_0(r)$ may be defined as

$$T_0^{00} = \rho_0(r) \quad (27)$$

$$T_0^{11} = T_0^{22} = T_0^{33} = P_0(r) \quad (28)$$

The only observable component of stress for a local observer will be the proper hydrostatic pressure. It follows that the energy-momentum tensor becomes

$$T^{\mu\nu} = \frac{\partial x^\mu}{\partial x_0^0} \frac{\partial x^\nu}{\partial x_0^0} \rho_0 + \frac{\partial x^\mu}{\partial x_0^1} \frac{\partial x^\nu}{\partial x_0^1} P_0 + \frac{\partial x^\mu}{\partial x_0^2} \frac{\partial x^\nu}{\partial x_0^2} P_0 + \frac{\partial x^\mu}{\partial x_0^3} \frac{\partial x^\nu}{\partial x_0^3} P_0 \quad (29)$$

where $x_0^0, x_0^1 \dots$ are 'proper' coordinates and $x^0, x^1 \dots$ are the points of interest. Also

$$g^{\mu\nu} = \frac{\partial x^\mu}{\partial x_0^\alpha} \frac{\partial x^\nu}{\partial x_0^\beta} g_0^{\alpha\beta} \quad (30)$$

reduces to

$$\frac{dx^\mu}{ds} = \frac{\partial x^\mu}{\partial x_0^0} \quad (31)$$

Inserting (31) into (29) gives

$$\begin{aligned} T^{\mu\nu} &= (\rho_0 + P_0) \frac{dx^\mu}{ds} \frac{dx^\nu}{ds} - g^{\mu\nu} P_0 \\ \therefore T_\mu^\nu &= (\rho_0 + P_0) g_{\alpha\mu} \frac{dx^\alpha}{ds} \frac{dx^\nu}{ds} - g_\mu^\nu P_0 \end{aligned} \quad (32)$$

In our static case we have

$$\frac{dt}{ds} = e^{-\frac{\nu}{2}} \quad (33)$$

$$\frac{dr}{ds} = \frac{d\theta}{ds} = \frac{d\phi}{ds} = 0 \quad (34)$$

which leads to

$$T_0^0 = \rho_0 \quad (35)$$

$$T_1^1 = T_2^2 = T_3^3 = -P_0 \quad (36)$$

From (36), (25) and (23) we arrive at the relativistic solution for hydrostatic equilibrium

$$\frac{dP_0}{dr} + (\rho_0 + P_0) \frac{\nu'}{2} = 0 \quad (37)$$

which is comparable to the Newtonian solution (3).

3.1.1 Exterior Solution (Schwarzschild)

In empty space, all components of T_μ^ν are zero. So by relating $T_0^0 = T_1^1$ (23) and (24), it is clear that $\lambda' = -\nu'$. Again, relating to T_2^2 (25) it follows that

$$\nu'' + \nu'^2 + \frac{2\nu'}{r} = 0 \quad (38)$$

which has a solution in the form

$$e^\nu = a + \frac{b}{r} \quad (39)$$

Using the special relativity metric and restoring the correct units

$$e^{-\lambda} = 1 - \frac{2GM}{c^2 r} \quad (40)$$

where M is the total mass.

3.1.2 Interior Solution (Oppenheimer and Volkoff)

This solution was originally formulated in [44] as a means to explore the physics of massive neutron cores. Due to the presence of the fermions, we can no longer make the equality between (23), (24) and (25) as in the exterior solution, T_μ^ν is now non-zero. By using a trial and error approach and introducing a variable which has the form

$$u(r) = \frac{r}{2} (1 - e^{-\lambda}) \quad (41)$$

the T_0^0 solution (23) then becomes

$$\frac{du}{dr} = 4\pi\rho_0 r^2 \quad (42)$$

At the outer radius (R , which must be continuous with the exterior solution), we see that

$$u_R = \frac{R}{2} (1 - e^{-\lambda(R)}) = M \quad (43)$$

So the solution to $e^{-\lambda}$ is the same for both the interior and the exterior (40). Re-inserting the correct units, T_1^1 (24) becomes

$$\frac{dP_\nu}{dr} = -\frac{G}{r^2} \left(\frac{\rho_0 + \frac{P_\nu}{c^2}}{r - 2u} \right) \left(m + \frac{4\pi P_\nu r^3}{c^2} \right) \quad (44)$$

3.2 Equation of State for a Relativistic Degenerate Fermi Gas

This is by far the simplest approach to derive the equation of state for a relativistic degenerate Fermi gas [45]. We begin by confining N fermions in a volume V . The number of quantum states with momentum between p and $p + dp$ is given by

$$\frac{4V\pi g_\nu p^2 dp}{h^3} \quad (45)$$

Pauli's exclusion principle implies

$$N(p)dp \leq \frac{4V\pi g_\nu p^2 dp}{h^3} \quad (46)$$

A completely degenerate gas has all lowest states occupied

$$N(p) = \frac{4V\pi g_\nu p^2}{h^3} \quad (47)$$

If there is a finite number N of fermions, then they must all have momentum less than the Fermi momentum p_0 such that

$$N = \frac{4V\pi g_\nu}{h^3} \int_0^{p_0} p^2 dp = \frac{4V\pi g_\nu p_0^3}{3h^3} \quad (48)$$

The Fermi momentum is related to number density by

$$n = \frac{N}{V} = \frac{4\pi g_\nu p_0^3}{3h^3} \quad (49)$$

The pressure is the mean rate of transfer of momentum across an ideal surface of unit area, from this we obtain

$$PV = \frac{1}{3} \int_0^\infty N(p) p v_p dp \quad (50)$$

where v_p is the associated velocity, this leads to

$$P = \frac{4\pi g_\nu}{3h^3} \int_0^{p_0} p^3 \frac{\partial E}{\partial p} dp \quad (51)$$

The internal energy of the gas (due to translational energy of the motions of individual fermions) is

$$U = \int_0^\infty N(p) E dp \quad (52)$$

for complete degeneracy we get

$$U = \frac{4V\pi g_\nu}{h^3} \int_0^{p_0} E p^2 dp \quad (53)$$

$$\therefore P = \frac{4\pi g_\nu}{3h^3} E(p_0) p_0^3 - \frac{U}{V} \quad (54)$$

and according to special relativity

$$E = mc^2 \left(\sqrt{1 + \frac{p^2}{m_\nu^2 c^2}} - 1 \right) \quad (55)$$

$$\frac{\partial E}{\partial p} = \frac{1}{m_\nu} \left(1 + \frac{p^2}{m_\nu^2 c^2} \right)^{-\frac{1}{2}} p \quad (56)$$

Inserting into (51) we arrive at

$$P = \frac{4\pi g_\nu}{3m_\nu h^3} \int_0^{p_0} \frac{p^4 dp}{\sqrt{1 + \frac{p^2}{m_\nu^2 c^2}}} \quad (57)$$

By substituting $\sinh \theta = \frac{p}{mc}$ we get

$$\begin{aligned} P &= \frac{4\pi g_\nu m_\nu^4 c^5}{3h^3} \int_0^{\theta_0} \sinh^4 \theta d\theta \\ &= \frac{4\pi g_\nu m_\nu^4 c^5}{3h^3} \left[\frac{\sinh^3 \theta \cosh \theta}{4} - \frac{3 \sinh 2\theta}{16} + \frac{3\theta}{8} \right]_{\theta=\theta_0} \end{aligned} \quad (58)$$

By making the following substitution, in order that we may use a more convenient unit in dealing with Fermi momentum

$$X = \frac{p_0}{m_\nu c} \quad (59)$$

and using $\sinh^{-1} X = \ln(X + \sqrt{1 + X^2})$, (58) reduces to

$$P = K \left[X (1 + X^2)^{\frac{1}{2}} \left(\frac{2}{3} X^2 - 1 \right) + \ln \left(X + (1 + X^2)^{\frac{1}{2}} \right) \right] \quad (60)$$

where

$$K = \frac{g_\nu m_\nu^4 c^5}{16\pi^2 h^3} \quad (61)$$

Noting that the mass energy density is given by the internal energy density plus the addition of all the fermion rest mass energies, we get

$$\rho = \frac{U}{Vc^2} + nm \quad (62)$$

Working from (62), (54) and (49) we obtain the relativistic equation of state for a Fermi gas, concerning the proper mass density

$$\rho = \frac{K}{c^2} \left[X (2X^2 + 1) (1 + X^2)^{\frac{1}{2}} - \ln \left(X + (1 + X^2)^{\frac{1}{2}} \right) \right] \quad (63)$$

Equations (60), (61) and (63) fulfil our requirements for the degenerate relativistic equation of state for a Fermi gas.

3.3 Mass Distribution

Now that we have formulated the equation of hydrostatic equilibrium and the equation of state for a degenerate relativistic Fermi gas, we may combine them in order to find the mass distribution of the fermion ball. By using the dimensionless units

$$x = \frac{r}{b_\nu} \quad \mu = \frac{m}{d_\nu} \quad (64)$$

where

$$b_\nu = \sqrt{\frac{4\pi\hbar^3}{Gg_\nu m_\nu^4 c}} \quad d_\nu = 2\sqrt{\frac{4\pi\hbar^3 c^3}{G^3 g_\nu m_\nu^4}} \quad (65)$$

It is possible to obtain the mass distribution from (44), (61) and (63) by integrating over the density as in the Newtonian solution (14).

$$\begin{aligned} \frac{dX}{dx} = & -\frac{1+X^2}{X(x^2-2\mu x)} \\ & \left\{ \mu + x^3 \left[X(1+X^2)^{\frac{1}{2}} \left(\frac{2}{3}X^2 - 1 \right) + \ln \left(X + (1+X^2)^{\frac{1}{2}} \right) \right] \right\} \end{aligned} \quad (66)$$

$$\frac{d\mu}{dx} = x^2 \left\{ X(1+X^2)^{\frac{1}{2}} (2X^2 + 1) - \ln \left(X + (1+X^2)^{\frac{1}{2}} \right) \right\} \quad (67)$$

And again, as in the Newtonian case, these equations must be solved numerically. As we have no need for inserting a baryon core, we simply set $\mu(x_0) = 0$ and select a value for the Fermi momentum $X(x_0)$. This allows for calculation of the total mass and radius of the fermion ball from a single parameter (besides the fermion characteristics), but has the disadvantage of requiring a trial and error technique when selecting total mass. Solutions for X , μ and μ' are presented in Figure 10.

It is enlightening to find that the relativistic derivation of the mass distribution has confirmed the classical method. For this reason, graphs of mass distribution will not be shown as they are identical to those in Section 2. However, the relativistic approach has been useful, as it has also revealed more information about the fermion ball. It is now possible to plot a relativistic relation between total mass and radius (Figure 11) and has also given an alternative numerical technique for calculating M and M' , in fact this method turns out to be preferred in the spectra simulations of Section 6.

It is clear from the mass-radius plot that the fermion ball is indeed non-relativistic, as relativistic effects are only prevalent near the Oppenheimer-Volkoff limit, which is a factor of 10^3 larger than the mass of the centre of our galaxy. The Oppenheimer-Volkoff limit is the maximal mass which a degenerate fermion ball can have. It is noteworthy that this Oppenheimer-Volkoff limit is very much comparable to the mass of the largest observed super-massive, compact, dark object which is $3 \times 10^9 M_\odot$; M87 in the Virgo cluster [1].

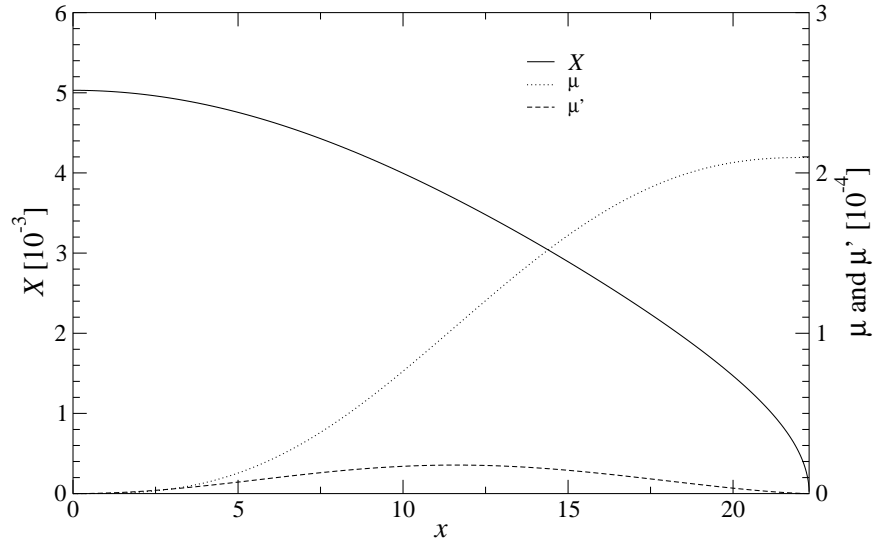


Figure 10: Relativistic solution of the dimensionless mass μ , derivative μ' and Fermi momentum X as functions of the dimensionless radius.

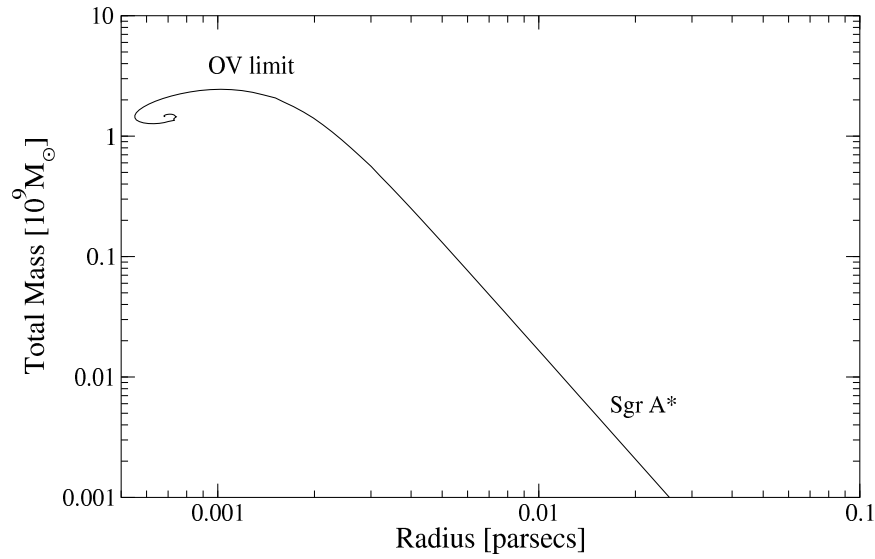


Figure 11: Relativistic mass-radius relation. Note the turning point is the Oppenheimer-Volkoff limit ($2.45 \times 10^9 M_\odot$) and the curve left of the maximum represents unstable configurations curling around the point of infinite central density. The mass-radius region which the centre of our galaxy lies within is noted as Sgr A*. As previously decided upon, this is for 16keV, $g_\nu = 2$ fermions.

4 Formation of a Fermion Ball

*We are all agreed that your theory is crazy.
The question which divides us is whether it is
crazy enough to have a chance of being correct.
– Niels Bohr*

Thus far, we have argued that a fermion ball is possible, provided a 16keV fermion exists in nature. Candidates for such a fermion and their origins have also been briefly mentioned. Another requirement of the theory is that such a fermion ball may be formed. This section aims to show that it is possible to create such an object by closely following the work of [35].

4.1 Analogy to a Boson Star

To understand the formation of a fermion ball, we first study the analysis of self-interacting scalar fields, often called boson stars [36]. We then use scaling arguments to make an equivalence to a certain type of cold boson star.

Consider a complex scalar field Ψ with a repulsive Lagrangian interaction term $U(|\Psi|^2)$. By introducing the dimensionless parameter Λ , we define the length and mass scales as

$$R_* = \frac{\Lambda}{m} = \frac{\lambda m_{pl}}{m^2} \quad M_* = R_* m_{pl}^2 \quad (68)$$

where $m_{pl} = \sqrt{G}^{-1}$ is the Planck mass. In the Newtonian limit, a self-gravitating boson star is governed by the dimensionless Gross-Pitaevskii like equations

$$\Delta\phi = |\Psi|^2 \quad (69)$$

$$\frac{i}{\Lambda} \frac{\partial \Psi}{\partial t} = \left[-\frac{\Delta}{2\Lambda^2} + \phi + V(|\Psi|^2) \right] \Psi \quad (70)$$

$$\rho = \frac{m^4}{4\pi\lambda^2} |\Psi|^2 \quad (71)$$

where we have introduced the dimensionless potential

$$V(|\Psi|^2) = \frac{4\pi\lambda^2}{m^4} \frac{dU}{d|\Psi|^2} \quad (72)$$

The pressure tensor in these dimensionless units is given by

$$P_{ij} = \frac{m^4}{4\pi\lambda^2\Lambda^2} \left(\text{Re} \frac{\partial \Psi}{\partial x_i} \frac{\partial \Psi^*}{\partial x_j} - \delta_{ij} \frac{\Delta |\Psi|^2}{4} \right) + \delta_{ij} \left(|\Psi|^2 \frac{dU}{d|\Psi|^2} - U \right) \quad (73)$$

A static, spherically symmetric solution is obtained with the ansatz

$$\Psi = e^{-i\epsilon R_* t} \Phi(r) \quad (74)$$

where $\Phi(r)$ is a real function. It is clear that for large Λ , (70) and (74) reduce to

$$\frac{\epsilon}{m} - \phi - V = 0 \quad (75)$$

This solution is exact in the limit $\Lambda \rightarrow \infty$, which is the Thomas-Fermi limit [37]. In this limit, (73) becomes diagonal with $P = P_{ii}$. We obtain an equation of state given by (71) and

$$P = \rho V(\rho) - U(\rho) \quad (76)$$

Equations (75) and (76) yield the equation of hydrostatic equilibrium

$$\frac{dP}{\rho} = -d\phi \quad (77)$$

If the equation of state is given as the polytropic type

$$P(\rho) = K\rho^{1+\frac{1}{n}} \quad (78)$$

we can determine the potential U and V by integrating (77). It can therefore be shown that Equation (77) is equal to V , which yields

$$V = (n+1)K\rho^{\frac{1}{n}} \quad (79)$$

If we fix λ in a convenient manner, we get the potential

$$V = |\Psi|^{\frac{n}{2}} \quad (80)$$

The polytropic equation of state with $n = \frac{3}{2}$, together with (77) and (69) (the dimensionless Poisson equation), describe a fermion ball. This has demonstrated that a fermion ball is equivalent to a boson star in the limit $\Lambda \rightarrow \infty$. It has been shown numerically [36] that even for moderate values of Λ , the static solutions are almost degenerate and are quite well approximated by the static solution for an infinite Λ .

4.2 Time Evolution of the Collapse

The basic regulating mechanism is the kinetic part of (70), which penalises density spikes. The criterion for simulation is that the ratio of kinetic and pressure contributions to the static energy functional should be small. Great care must be taken during numeric simulation to ensure that the self-interaction term V is not dominated by the other terms. If this occurs, there is a crossover to mini boson star behaviour.

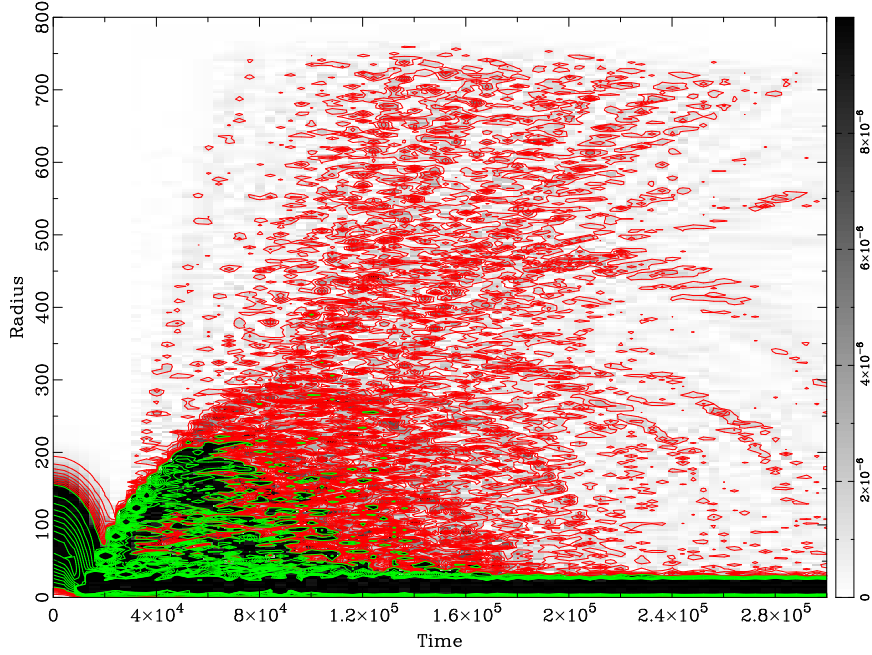


Figure 12: Combined contour-density plot for the evolution of $|r\Psi|^2$. Green contour lines denote levels from 10^{-5} to 10^{-4} while red lines denote levels below 10^{-5} . Gravitational collapse is followed by an ejection of excess matter leaving a fermion ball at the centre [35].

An evolution plot for collapsing fermionic matter ball is shown in Figure 12. To prevent matter from being artificially reflected by the radius boundary, an r -dependant imaginary ‘sponge’ has been introduced. This sponge removes the ejected fermionic matter.

In summary, using a bosonic representation of the dynamical Thomas-Fermi theory for a self-gravitating gas, it can be shown that non-relativistic, degenerate fermionic matter will form a super-massive fermion ball through gravitational collapse accompanied by ejection.

5 Dynamics of Stars near the Galactic Centre

*The computer can't tell you the emotional story.
It can give you the exact mathematical design,
but what's missing are the eyebrows.
– Frank Zappa*

The best way to probe a distribution of mass when it does not emit very strongly, is to observe the orbits of objects moving through that distribution. Luckily the orbits of stars near the centre of the galaxy have been spatially resolved [38, 39] and we may therefore use this data to compare with motion predictions from computer simulations using the fermion ball mass distribution. But as there are a lot of stars neighbouring the central object, we must first decide which to concentrate our efforts upon. Throughout the calculations, we assume that the central object is incident with the radio source Sgr A*, and use 16keV, $g_\nu = 2$ fermions.

5.1 Closed and Precessing Orbits

By nature, a point source object will produce a closed orbit, whereas a mass distribution will in general produce a precessing open orbit. This precession is clearly a definite way to tell (over time) if the stars near Sgr A* are orbiting around a central black hole or within a mass distribution. In order for this method of discernment to be valid, the stars must move within the fermion ball. In addition, the stars must not possess velocities greater than the escape velocity of the black hole. For clarity, black hole solutions are often abbreviated to BH and those of the fermion ball to FB. The escape velocity (escape to infinity) is given by

$$v_{esc} = \sqrt{2\Phi} \quad (81)$$

while the circular velocity is

$$v_{cir} = \sqrt{\frac{GM(r)}{r}} \quad (82)$$

Using data from [3] made in 1996.58, Figure 13 shows the observed velocities from proper motion analysis alongside the calculated escape and circular velocities for the black hole and fermion ball scenarios.

There are two schools of thought on the naming conventions of the stars near Sgr A* [38, 39], and the numbers often contradict (e.g. S0-4 is also S8). We shall use the 2-digit notation where the first number suggests the distance band which the star falls within, e.g. S0-1, S0-2... are all within 1" of Sgr A*, and S1-1, S1-2... within the 1" to 2" range, and so on.

S0-3 is suspected to have a very large position component in our line of sight (due to it's near 'straight line' trajectory) and is therefore ruled out

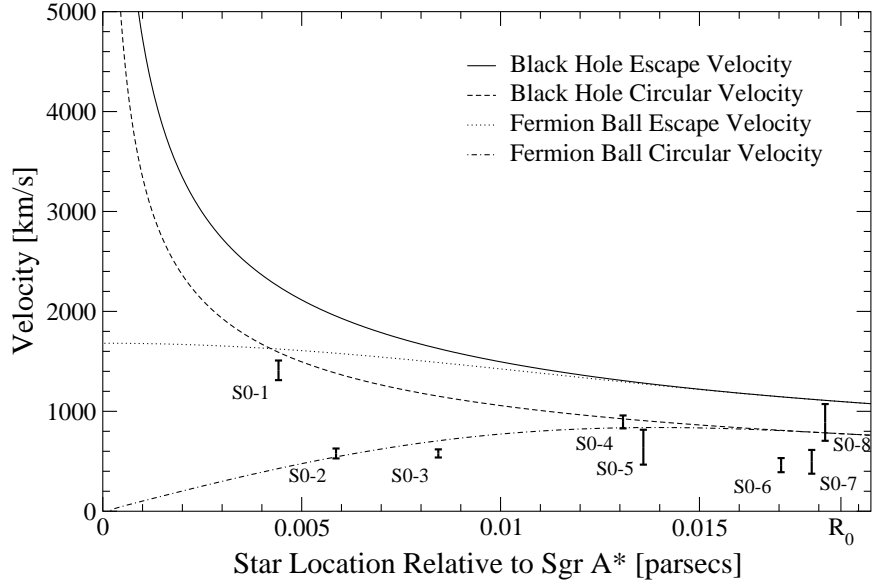


Figure 13: Velocities from proper motion analysis [3] alongside the calculated escape and circular velocities for the black hole and fermion ball scenarios. Fermion ball radius noted as R_0 . This plot is made using the position and velocity vectors as calculated from the right ascension and declination data. There is no data available in our line of sight, thus all points are minimal values. Epoch 1996.58.

as an object of interest. However, from Figure 13 it is clear that the stars S0-1 through S0-5 may be within the projected radius of the fermion ball. However, of those stars, only S0-1, S0-2 and S0-4 have been identified as being on accelerating orbits. We will therefore use these 3 stars to draw comparisons with models of motion.

5.2 Newtonian Motion

We calculate the trajectories of the stars by solving Newton's equations of motion in 3-dimensions

$$\begin{aligned}
 \frac{d^2x}{dt^2} &= -\frac{GM(r)}{(x^2 + y^2 + z^2)^{\frac{3}{2}}}x \\
 \frac{d^2y}{dt^2} &= -\frac{GM(r)}{(x^2 + y^2 + z^2)^{\frac{3}{2}}}y \\
 \frac{d^2z}{dt^2} &= -\frac{GM(r)}{(x^2 + y^2 + z^2)^{\frac{3}{2}}}z
 \end{aligned} \tag{83}$$

where x, y, z are the distances from the origin in a Euclidean coordinate system centred on Sgr A*, taking x to be opposite the observed right ascension, y as the observed declination, and z to be the line of sight in the direction of the sun. The solution of the coupled differential equations (83) depends upon 7 initial conditions, which are the x, y, z position and velocity components with the mass of the central object as the final parameter. We first minimise the fit to initial x, y position and v_x, v_y velocity parameters, then run a χ^2 phase space analysis on the z position and velocity parameters. The effect of varying the central mass is briefly discussed afterwards using limits imposed by [3].

The data we choose to use consists of a combination of spatial analysis from 2 independent sources [38, 39] on the 3 stars S0-1, S0-2 and S0-4 over the observing period 1992.7 to 2000.5. The location of Sgr A* moves over time (against the background), fortunately the data has already considered this and all positions are relative to the location of Sgr A*. There are 36 data points for each star from 18 separate observations, which must be fitted. It is important to stress that the parameters already mentioned as initial conditions are for the 1992.7 epoch, and cannot be directly compared, to say, the data in Figure 13, which is the epoch 1996.58.

5.3 χ^2 Reduction of z and v_z

5.3.1 Notes on χ^2

A χ^2 analysis is the most commonly accepted method for comparing experimental data to a theoretical model, a smaller value signals a better fit to the experiment. A χ^2_{ndf} (χ^2 per number of degrees of freedom) is a more rigorous way to examine the fit as it will also consider the number of data points used and the number of free variables in the theory. The form of the data in this case is such that we must perform a separate χ^2 fit for both the x and y observed data, each given by

$$\chi_x^2 = \sum_{i=1}^N \frac{(x_i - \bar{x}(x, v_x, y, v_y, z, v_z, M))^2}{\sigma_{x_{err}}^2} \quad (84)$$

$$\chi_y^2 = \sum_{i=1}^N \frac{(y_i - \bar{y}(x, v_x, y, v_y, z, v_z, M))^2}{\sigma_{y_{err}}^2} \quad (85)$$

These χ^2 values can safely be added linearly as the nature of χ^2 is such that it need not be added in quadrature (as the χ itself will already be added in quadrature). The total χ^2 , which is the quantity of interest can then be written as

$$\chi^2 = \chi_x^2 + \chi_y^2 \quad (86)$$

and the χ^2 per number of degrees of freedom is

$$\chi_{ndf}^2 = \frac{\chi^2}{N - N_p} \quad (87)$$

where $N = 36$ and $N_p = 7$.

Simulations of star dynamics were performed several times in order to minimise the χ^2 for initial parameters x , v_x , y and v_y , but by no means have the χ^2 been fully reduced. Computing time restricted the iterations of the simulations to 4 passes, and further iterations would most certainly produce slightly smaller χ^2 .

The astronomical unit of arcsec has been preferred in the presentation of the results as this is the unit used during observations. This unit system may appear unusual when referring to the z axis which is in the observer's line of sight, but it can be thought of as being equivalent to the distance projected at a fixed distance of 8kpc, as can the x and y axis.

5.3.2 Best Fits

By first minimising the initial x and y position and velocity parameters, this allows for a χ_{ndf}^2 phase space plot of the unknown z position and velocity parameters. Table 1 lists the minimal χ_{ndf}^2 for each of the 3 stars in each scenario. Figures 14 through 19 are the phase space plots, using colour as the 3rd dimension. In order to ensure a high resolution in the data representation, each plot is a result of 22,000 runs of the simulation. There has been no interpolation performed on the images.

Table 1 reveals that the fits for S0-1 have a much higher χ_{ndf}^2 compared with S0-2 and S0-4. This is due to inconsistencies within the experimental data. Figures 20 through 24 show the x and y paths of the stars for each of the reduced χ_{ndf}^2 scenarios. Extra paths are also shown for bound orbits, where the minimum fit χ_{ndf}^2 is an unbound orbit. These tables highlight the numerically minimal χ^2 values for each plot, but as can be seen clearly from figures 14 through 19, the minimal χ^2 is not always well defined and the z , v_z values may take on a much larger range only expressible in the plots.

The inconsistencies within the S0-1 data can be clearly seen in Figure 20, possibly due to the discernment of 'north' not agreeing between each of the data sources, resulting in a 'rotation' effect.

Similar fits were also obtained for the extremal masses of Sgr A*, with similar $z - v_z$, χ_{ndf}^2 phase space plots. Tables 2 and 3 show the minimal χ_{ndf}^2 fits. The mass does not appear to affect either scenario greatly and is the parameter of least impact to the fit. Re-iteration would again, certainly reduce the χ_{ndf}^2 slightly.

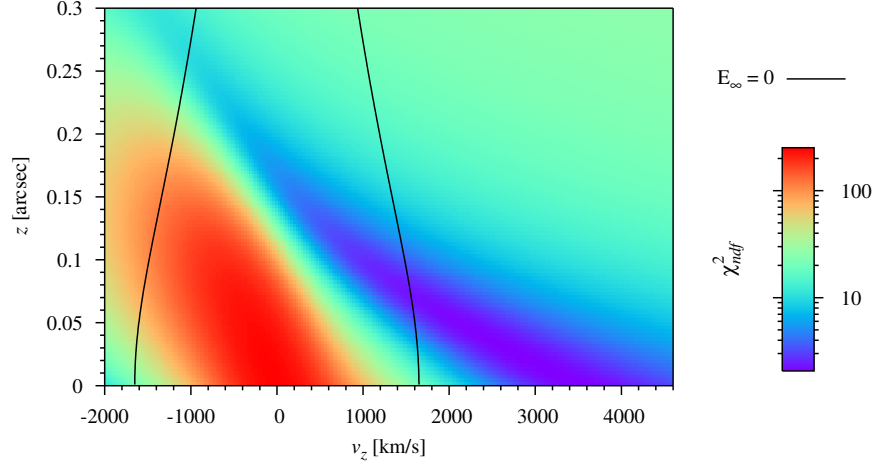


Figure 14: χ^2_{ndf} phase space plot for S0-1 with black hole. The lines represent the escape velocity required of the v_z component only, bound orbits being within the lines and unbound orbits outside. Epoch 1992.7.

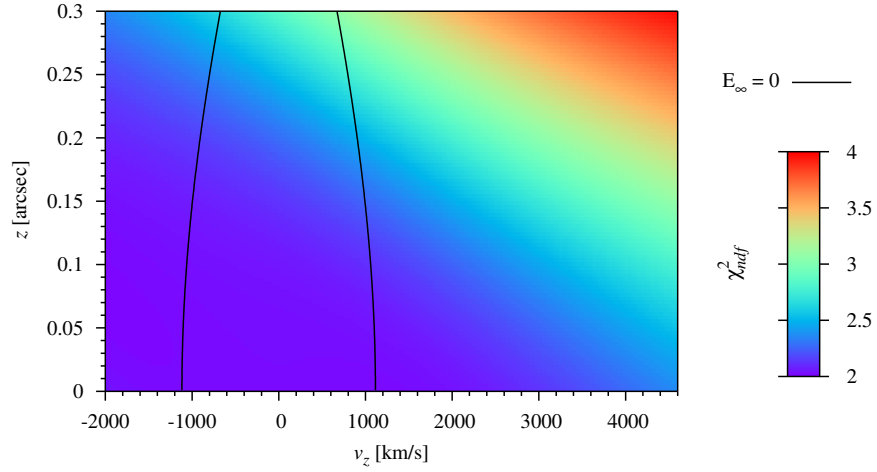


Figure 15: χ^2_{ndf} phase space plot for S0-1 with fermion ball. Epoch 1992.7.

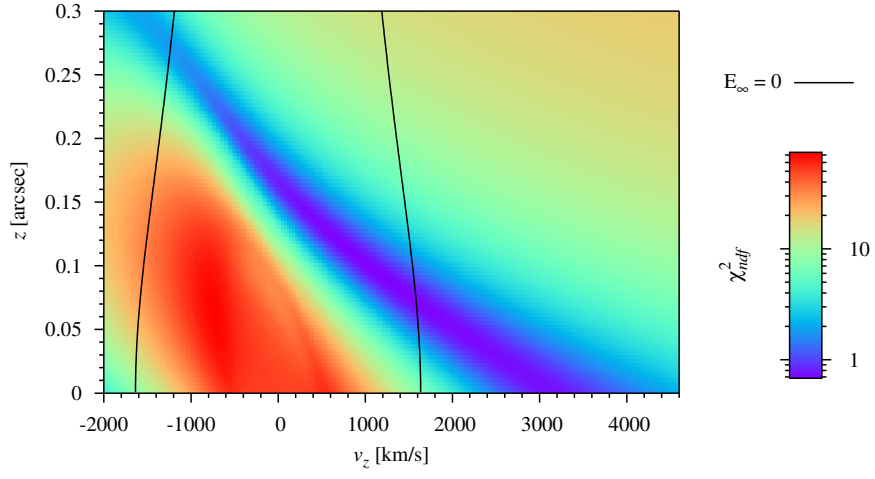


Figure 16: χ_{ndf}^2 phase space plot for S0-2 with black hole. Epoch 1992.7.

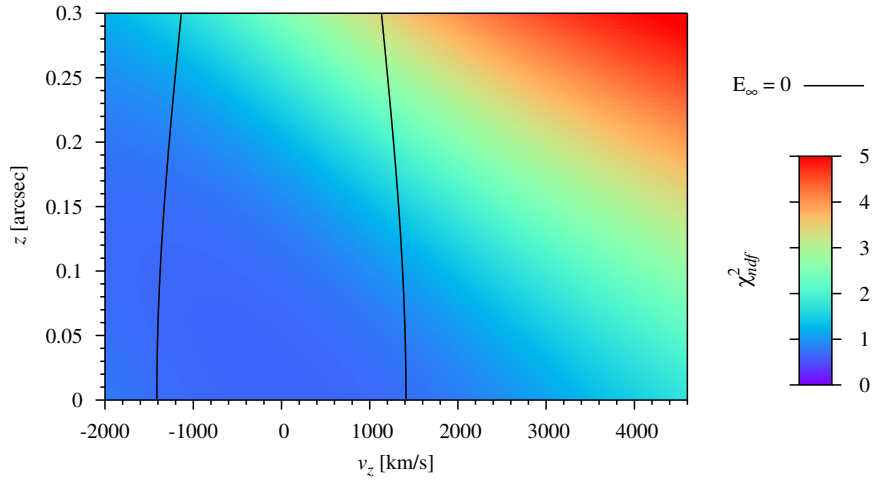


Figure 17: χ_{ndf}^2 phase space plot for S0-2 with fermion ball. Epoch 1992.7.

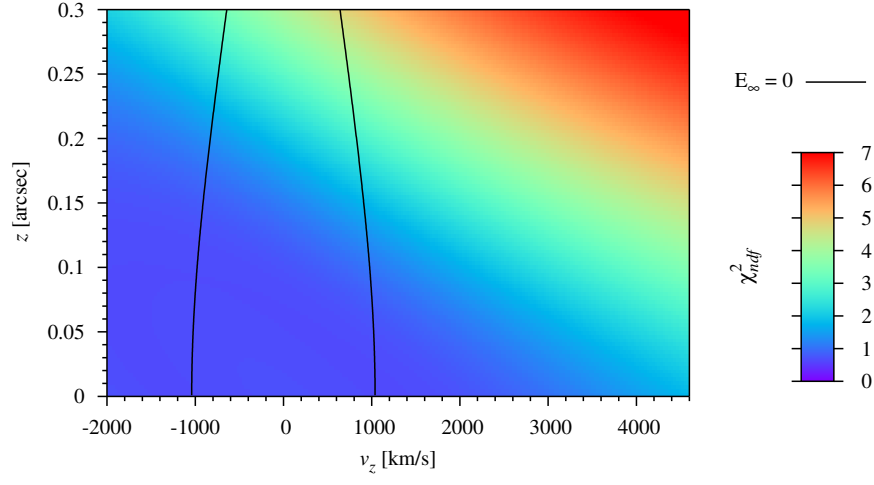


Figure 18: χ^2_{ndf} phase space plot for S0-4 with black hole. Epoch 1992.7.

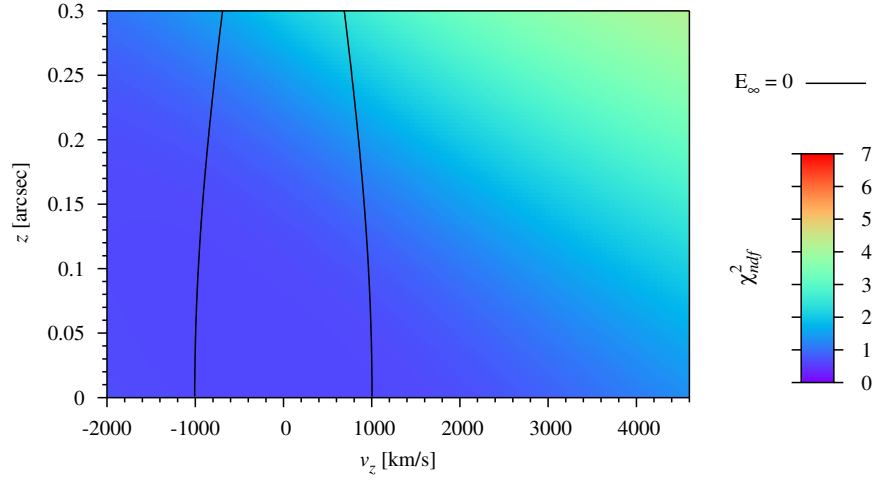


Figure 19: χ^2_{ndf} phase space plot for S0-4 with fermion ball. Epoch 1992.7.

5.4 Analysis

It is quite clear from Figures 14 through 19 that the fermion ball scenario applies much less constraints with selection of z and v_z initial conditions than the black hole scenario, which has quite rigid constraints. Accurate measurements of these parameters would most certainly be able to show if the black hole scenario describes the orbits sufficiently. However, experimental complications in taking said measurements make this an unlikely method of discernment in the near future.

Due to the likeness of Figures 18 and 19, we can clearly see that phase space analysis on S0-4 is unlikely to be able to tell us much about the mass structure of the galactic centre. As the star would be located on the outer edge of the fermion ball, the enclosed mass is almost that of the black hole, and the resulting dynamics are therefore very similar to those of the black hole scenario. However, if S0-4 re-enters the fermion ball, a precessing orbit will be produced, and this will be observable over time. Also, it is possible that S0-4 may travel incredibly close (within a milliparsec) of the black hole during the course of its orbit, for Figure 21 this occurs at around 2047. It may then be possible to observe relativistic effects upon the star's spectra, assuming the technology to resolve these spectra will improve by that time. Obviously these effects would not be present in the fermion ball scenario.

Observing the orbits of S0-1 and S0-2 will most certainly be a way to tell whether the galactic centre is a point source (black hole) or an extended source. Unfortunately, the observations need to be made over a much longer timescale in order to see possible orbital precession. S0-2 appears to show promise more quickly, allowing for discernment of any z - v_z combination within a maximum of 30 years. Data for z and v_z would certainly aid this process, and dramatically reduce the required observing time.

Star	x	v_x	y	v_y	z	v_z	χ_{ndf}^2	Orbit
S0-1 BH	0.125	0	0.105	-900	0.012	3190	2.06	unbound
S0-1 FB	0.121	-200	0.110	-1080	0.072	-1940	2.02	unbound
S0-2 BH	-0.028	300	0.200	-300	0.099	1090	0.68	bound
S0-2 FB	-0.028	300	0.200	-450	0.000	40	0.65	bound
S0-4 BH	-0.250	-800	-0.120	-600	0.000	-1190	0.68	unbound
S0-4 FB	-0.250	-760	-0.116	-600	0.072	-410	0.65	bound

Table 1: Minimal χ_{ndf}^2 for orbits of stars near the galactic centre. Final column notes a bound or unbound orbit using the escape velocity for that scenario, the number of degrees of freedom is 29. Positions are in arcsec and velocities, km/s. All initial parameters are for epoch 1992.7 and for a mass of $2.6 \times 10^6 M_\odot$.

Star	x	v_x	y	v_y	z	v_z	χ_{ndf}^2	Orbit
S0-1 BH	0.125	0	0.105	-900	0.000	3220	2.06	unbound
S0-1 FB	0.121	-200	0.110	-1080	0.000	40	2.10	bound
S0-2 BH	-0.028	300	0.200	-300	0.087	1120	0.68	bound
S0-2 FB	-0.028	300	0.200	-450	0.000	40	0.83	bound
S0-4 BH	-0.250	-800	-0.120	-600	0.000	40	0.69	bound
S0-4 FB	-0.250	-760	-0.116	-600	0.000	40	0.70	bound

Table 2: Minimal χ_{ndf}^2 for orbits of stars near the galactic centre of mass $2.4 \times 10^6 M_\odot$.

Star	x	v_x	y	v_y	z	v_z	χ_{ndf}^2	Orbit
S0-1 BH	0.125	0	0.105	-900	0.024	3130	2.07	unbound
S0-1 FB	0.121	-200	0.110	-1080	0.000	2170	2.00	unbound
S0-2 BH	-0.028	300	0.200	-300	0.111	1060	0.68	bound
S0-2 FB	-0.028	300	0.200	-450	0.150	-860	0.63	bound
S0-4 BH	-0.250	-800	-0.120	-600	0.030	1450	0.68	unbound
S0-4 FB	-0.250	-760	-0.116	-600	0.159	-650	0.65	bound

Table 3: Minimal χ_{ndf}^2 for orbits of stars near the galactic centre of mass $2.8 \times 10^6 M_\odot$.

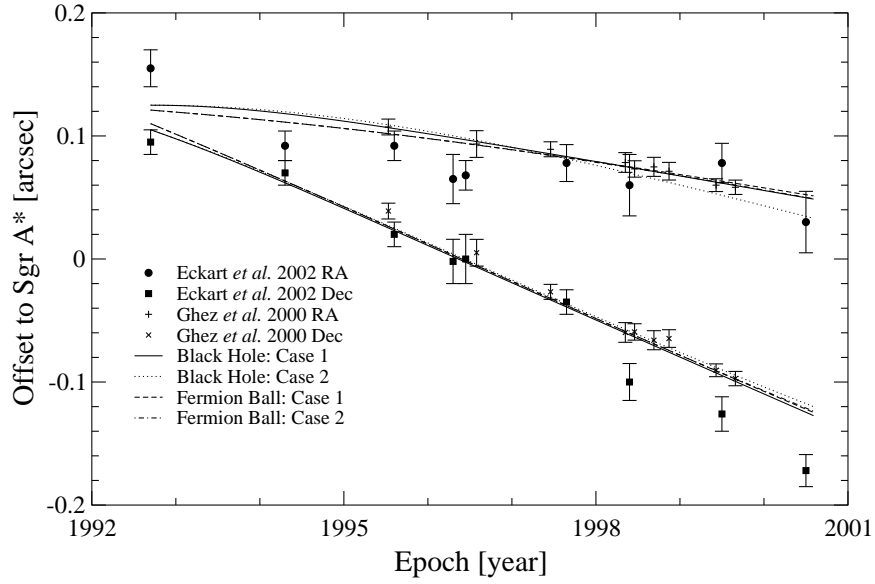


Figure 20: Best fits for S0-1. “Black Hole: Case 1” has $z=0.012\text{arcsec}$, $v_z=3190\text{km/s}$ with an unbound orbit and $\chi^2_{ndf} = 2.06$. “Black Hole: Case 2” has $z=0.075\text{arcsec}$, $v_z=1360\text{km/s}$ with a bound orbit and $\chi^2_{ndf} = 2.54$. “Fermion Ball: Case 1” has $z=0.072\text{arcsec}$, $v_z=-1940\text{km/s}$ with an unbound orbit and $\chi^2_{ndf} = 2.02$. “Fermion Ball: Case 2” has $z=0\text{arcsec}$, $v_z=0\text{km/s}$ with a bound orbit and $\chi^2_{ndf} = 2.03$.

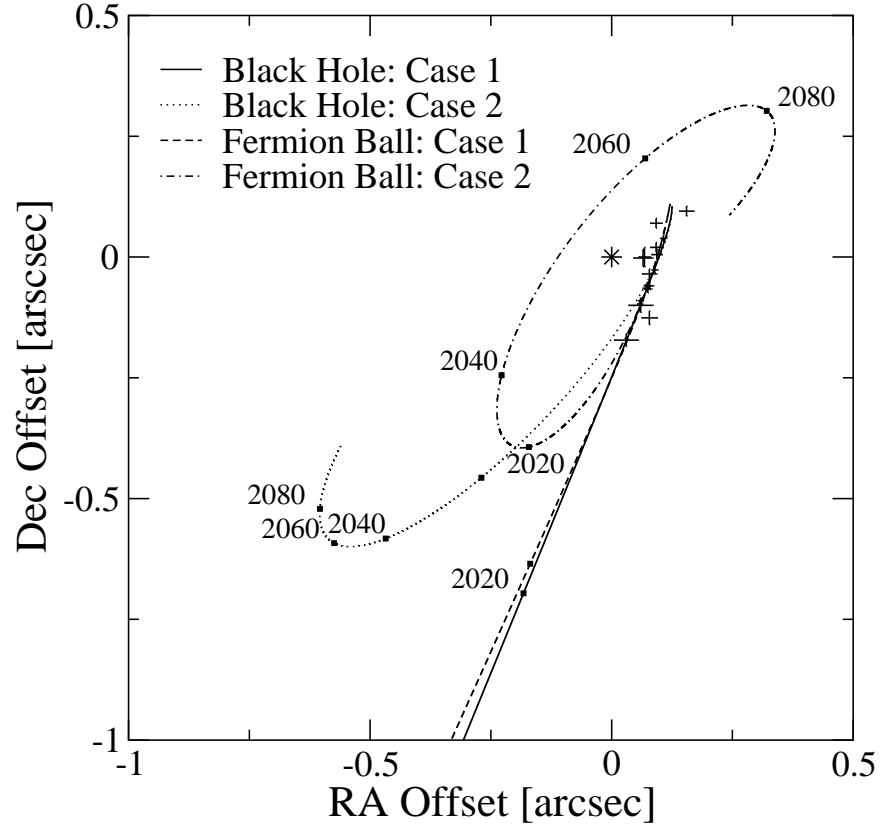


Figure 21: Best fits for S0-1, sky-plot projected until 2100. All cases carry the same initial conditions as Figure 20. The dynamic location of Sgr A* is denoted by the star.

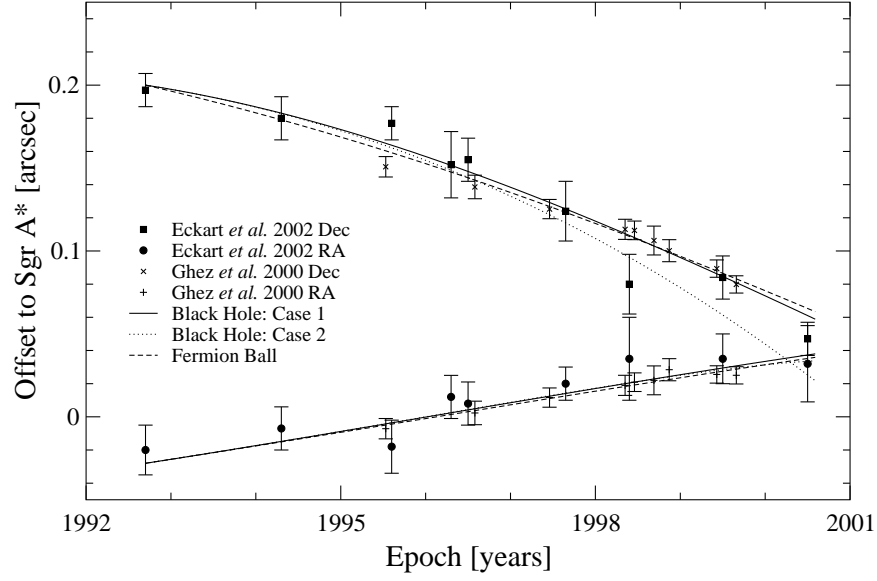


Figure 22: Best fits for S0-2. “Black Hole: Case 1” has $z=0.099\text{arcsec}$, $v_z=1090\text{km/s}$ with a bound orbit and $\chi^2_{ndf} = 0.68$. “Black Hole: Case 2” has $z=0.099\text{arcsec}$, $v_z=500\text{km/s}$ with a bound orbit and $\chi^2_{ndf} = 3.27$. “Fermion Ball” has $z=0\text{arcsec}$, $v_z=40\text{km/s}$ with a bound orbit and $\chi^2_{ndf} = 0.65$. “Black Hole: Case 2” has been chosen in order to describe a very tight orbit around Sgr A*.

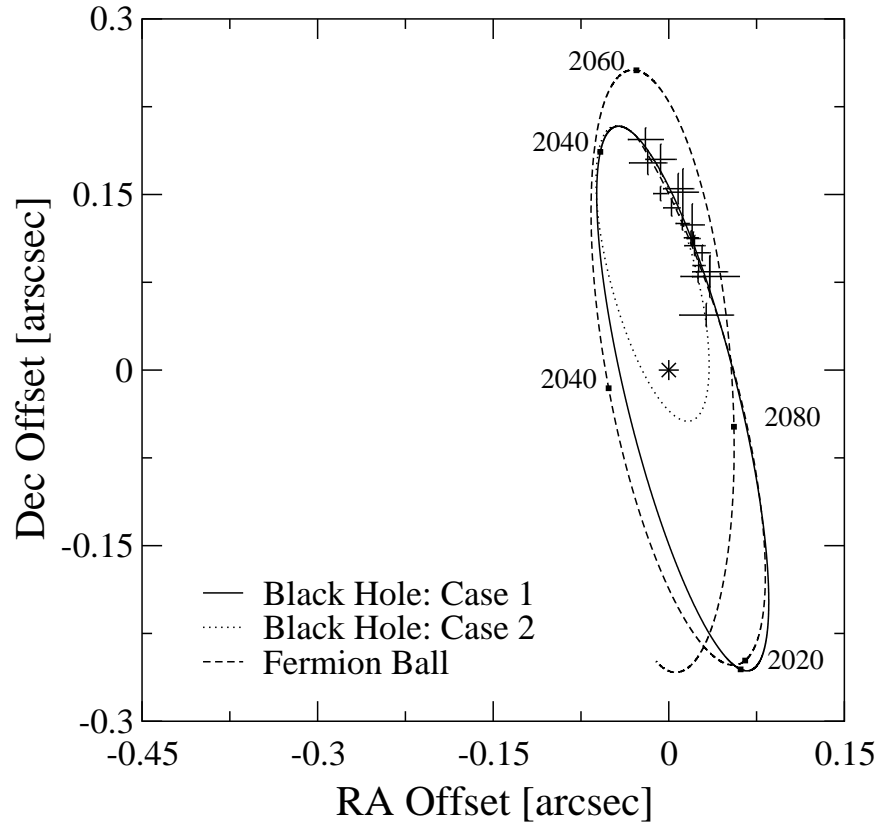


Figure 23: Best fits for S0-2, sky-plot projected until 2100. All cases carry the same initial conditions as Figure 22. The black hole case 1 has a bound orbital period of 50 years, case 2 of 20 years. The dynamic location of Sgr A* is denoted by the star.

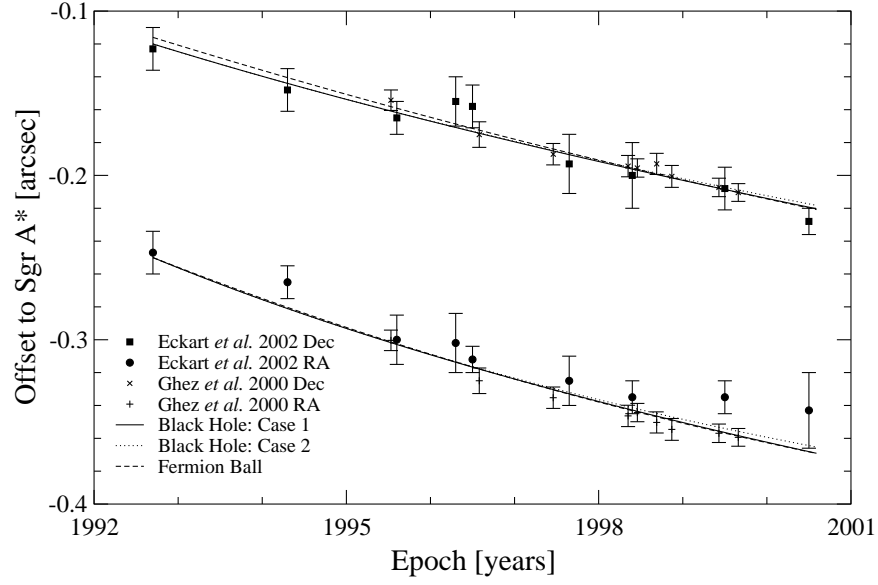


Figure 24: Best fits for S0-4. “Black Hole: Case 1” has $z=0\text{arcsec}$, $v_z=-1190\text{km/s}$ with an unbound orbit and $\chi^2_{ndf} = 0.68$. “Black Hole: Case 2” has $z=0\text{arcsec}$, $v_z=0\text{km/s}$ with a bound orbit of $\chi^2_{ndf} = 0.72$. The “Fermion Ball” case has $z=0.072\text{arcsec}$, $v_z=-410\text{km/s}$ with a bound orbit and $\chi^2_{ndf} = 0.65$.

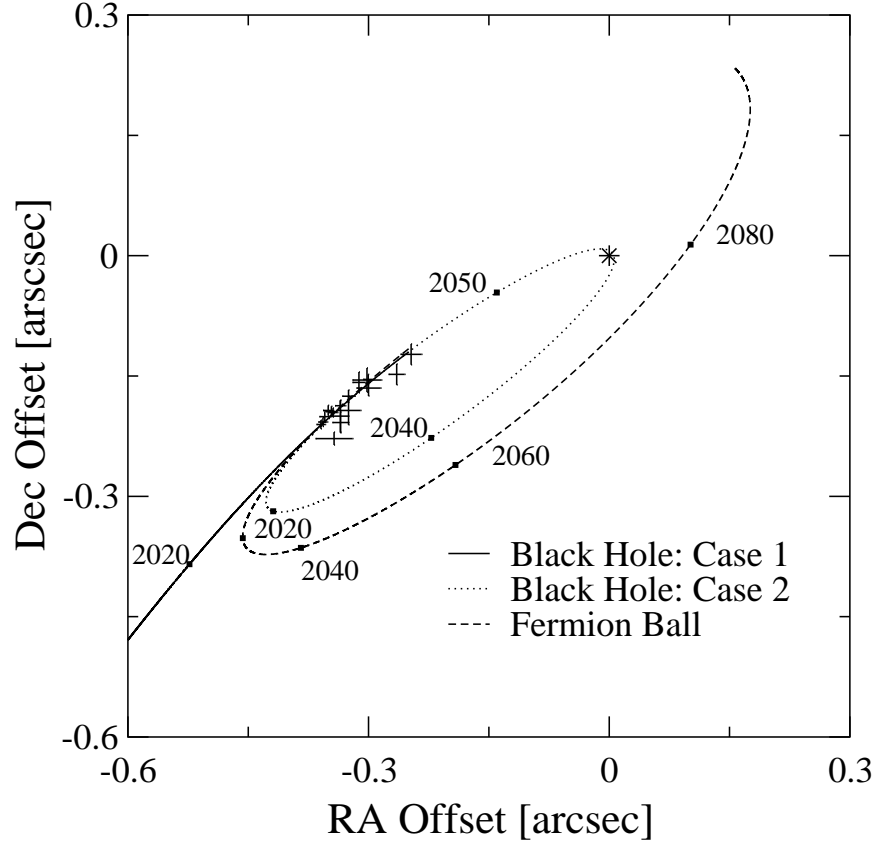


Figure 25: Best fits for S0-4, sky-plot projected until 2100. All cases carry the same initial conditions as Figure 24. “Black Hole: Case 2” has a bound orbital period of 60 years. The dynamic location of Sgr A* is denoted by the star.

5.5 The Importance of v_z and z

Since Newton's equations of motion (83) are time reflection invariant, it is possible to numerically solve the orbital paths back-wards in time. This allows for setting of initial parameters in any epoch. If accurate z or v_z data were to be made available in say 2005, it would constrain the χ^2 phase space plots for that epoch, dramatically reducing the required observing time needed for distinguishing black hole or mass distribution.

Several phase space plots are now presented for epoch 2005 (Figures 26 and 27), with initial parameters projected from the χ^2 reduction in Section 5.3.2. However, data fitting is restricted to pre 2000.5 (the most recent observation) and we have therefore assumed an orbital path up to our 'initial' start date of 2005.

It is clear from these plots that accurate z and v_z would instantly allow distinguishing between the 2 scenarios.

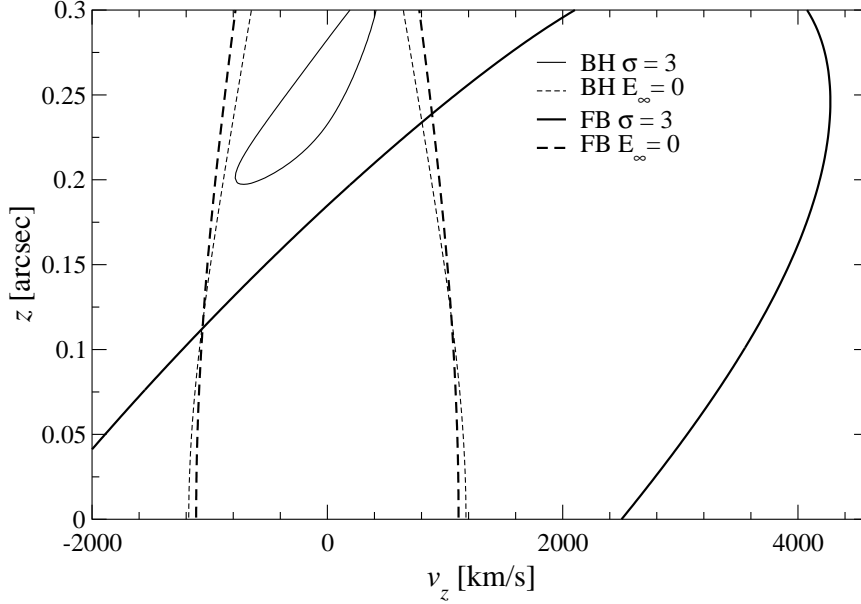


Figure 26: χ_{ndf}^2 phase space plot for S0-1 at epoch 2005. The paths for both “Case 2” scenarios in Figure 20 have been used to give the ‘initial’ position and velocity parameters for this plot (therefore we have assumed a bound orbit), values are in Table 4. Contour lines for $\chi_{ndf}^2=3$ are shown for both black hole and fermion ball scenarios, alongside the corresponding escape velocities. It is clear that the minimal χ_{ndf}^2 values for each scenario occupy different regions and therefore an accurate measurement of z or v_z would instantly allow one of the scenarios to be eliminated. For example a z measurement of 0.05arcsec would disallow the black hole scenario, similarly a z measurement of 0.25arcsec and v_z of 0km/s would rule out the fermion ball scenario.

Scenario	x	v_x	y	v_y
BH	-0.044	-656	-0.227	-822
FB	-0.007	-492	-0.233	-811

Table 4: Initial parameters for Figure 26. Epoch 2005. Positions are in arcsec and velocities, km/s.

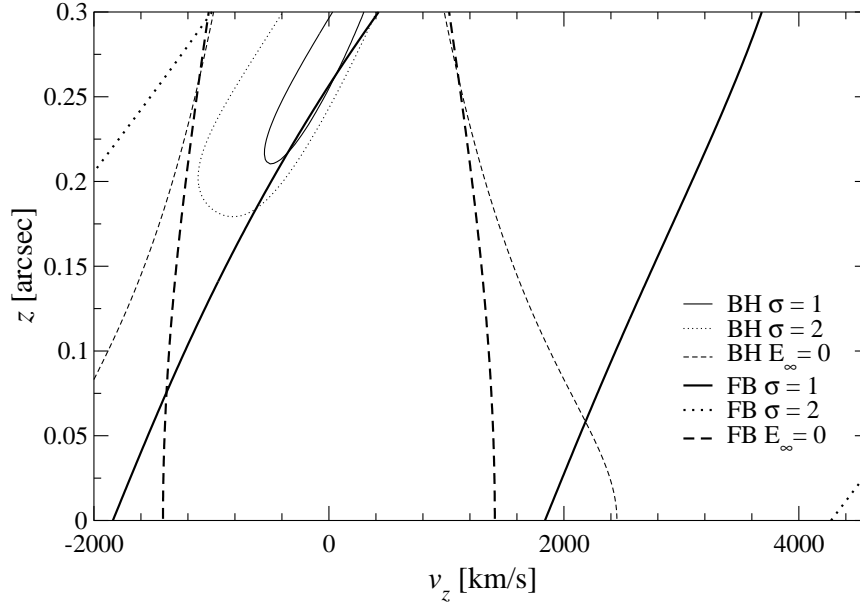


Figure 27: χ^2_{ndf} phase space plot for S0-2 at epoch 2005. The minimal χ^2 paths in Figure 22 have been used to give the ‘initial’ position and velocity parameters for this plot, values are in Table 5. Contour lines for $\chi^2_{ndf}=1$ and 2 are shown for both black hole and fermion ball scenarios, alongside the corresponding escape velocities. In this case, an accurate measurement of z or v_z may only allow for elimination of the black hole scenario, as the fermion ball minimal χ^2_{ndf} region is quite large.

Scenario	x	v_x	y	v_y
BH	-0.067	-196	-0.050	-922
FB	-0.064	-194	-0.035	-845

Table 5: Initial parameters for Figure 27. Epoch 2005. Positions are in arcsec and velocities, km/s.

6 Spectrum by Accretion of Matter

*Simulations are like miniskirts,
they show a lot, but hide the essentials.*
– Hubert Kirmann

The observed spectrum of the object at the centre of our galaxy is quite unusual. The spectrum seems to have no emission in the infra-red (IR) region, due to a very steep ‘cut-out’ between 10^{12} and 10^{13} Hz [46]. In this section, we investigate a very simple Newtonian accretion model [47], which assumes that the accretion disk is both geometrically thin and optically thick (we will return to the non-validity of this assumption later). We will show how a mass distribution, such as that of a fermion ball, will naturally produce this sudden drop in the accretion spectrum.

6.1 Source of the Accreting Gas

Radio continuum observations have revealed a ‘cometary tail’ of ionised gas from IRS7 (the brightest $2\mu\text{m}$ source in the central parsec of the galaxy) leading away from the the location of Sgr A*. The tail appears to be formed by a ‘circumnuclear’ wind which has been observed originating from the cluster of stars IRS16 (which is an IR source close to, but not incident with Sgr A*) [48]. This collision is highly supersonic and creates a bow-shock within the gas flows [51], see Figure 28. This bow-shock dissipates most of the directed kinetic energy and heats the gas to $7 \times 10^6 \text{K}$.

Assuming that Sgr A* is not itself the source of the gaseous outflow, we may treat this gas as an excellent candidate for accretion ‘fuel’ in powering the spectrum, observed from the central object. We assume the shocked plasma falls in radially toward the central object and that the accretion begins at radius R_a , given by the escape velocity

$$R_a = \frac{2GM}{v_{gw}^2} \quad (88)$$

where $v_{gw} = 500 \rightarrow 700 \text{ km/s}$. By simply comparing this velocity with Figure 13, we see that R_a is significantly outside the fermion ball such that this equation will result the same for both scenarios. Although the limits of accretion rate (\dot{M}) have been estimated in [51] as $3 \rightarrow 40 \times 10^{-3} M_\odot/\text{yr}$, it is widely accepted that the true values are much lower. The system is therefore much below the Eddington-limited accretion rate and is called ‘weakly accreting’. We also take the most probable inclination angle of the accretion disk as 60° .

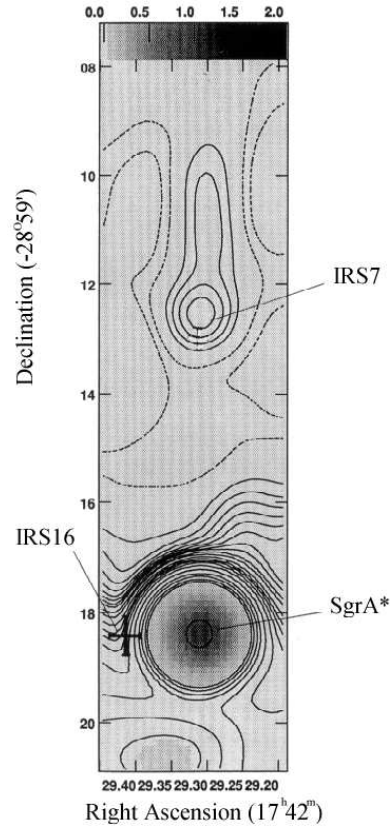


Figure 28: Contour map at $\lambda = 2\text{cm}$ of the IRS7 ‘cometary tail’ with relation to Sgr A*. The tail is a result of the collision between the galactic centre and stellar winds rather than from the motion of IRS7 through the interstellar medium [48].

6.2 Viscous Torque as a Means of Energy Release

Consider 2 shearing ‘rings’ in a gas of width λ , which meet at a surface of (radial) position R . Due to chaotic motions, gas elements are constantly exchanged across this surface with speeds $\simeq \tilde{v}$. A typical element travels a distance λ before interacting on the other side of the surface.

These elements of fluid carry slightly different amounts of angular momentum, corresponding to their location, either $R - \frac{\lambda}{2}$ or $R + \frac{\lambda}{2}$ (the substitutions $R_- = R - \frac{\lambda}{2}$ and $R_+ = R + \frac{\lambda}{2}$ are made for clarity). This process cannot result in any net transfer of matter between the rings as it occurs in equilibrium, therefore mass crosses the surface at equal rates in both directions of the order $\xi\tilde{v}$ per unit arc length, where ξ is the surface density.

As the elements each possess separate angular momenta, there is a net transfer due to the chaotic processes, a ‘viscous torque’ exerted on the outer stream by the inner, et vice versa. The fluid at $R - \frac{\lambda}{2}$ will appear (to an observer moving with the rings) to have velocity

$$R_- \Omega(R_-) - R \Omega(R) \quad (89)$$

and at $R + \frac{\lambda}{2}$

$$R_+ \Omega(R_+) - R \Omega(R) \quad (90)$$

Thus the average angular momentum ‘out’ (i.e. from inner ring to outer) is (per unit arc length)

$$R_- \tilde{v} \xi [R_- \Omega(R_-) - R \Omega(R)] \quad (91)$$

and ‘in’

$$R_+ \tilde{v} \xi [R_+ \Omega(R_+) - R \Omega(R)] \quad (92)$$

Since mass flow is the same in each direction, the net flux of momentum (assuming chaotic motions occur on a much shorter timescale than the angular velocity changes) can be written as

$$\tilde{v} \xi [R_-^2 \Omega(R_-) - R_- R \Omega(R) - R_+^2 \Omega(R_+) + R_+ R \Omega(R)] \quad (93)$$

and to first order

$$\begin{aligned} &= R^2 \tilde{v} \xi [\Omega(R_-) - \Omega(R_+)] \\ &= R^2 \tilde{v} \xi \lambda \frac{d\Omega}{dr} \\ &= \lambda R^2 \tilde{v} \xi \Omega' \end{aligned} \quad (94)$$

In an accretion disk, the rings are circular and we get the total torque by multiplying by the length $2\pi R$. The torque exerted by the outer ring on the inner is

$$G(R) = 2\pi R^3 \tilde{v} \xi \Omega' \quad (95)$$

where the coefficient of viscosity is $v = \lambda\tilde{v}$. Consider the net torque on a ring of gas between R and $R + \Delta R$. As this has an inner and outer edge, it is subject to shearing from both sides. The net torque is

$$G(R + dR) - G(R) = \frac{\partial G}{\partial R} dR \quad (96)$$

Because the torque is a result of the angular velocity, there is a rate of work

$$\Omega \frac{\partial G}{\partial R} dR = \left[\frac{\partial(G\Omega)}{\partial R} - G \frac{\partial \Omega}{\partial R} \right] dR \quad (97)$$

A simple summation will show that the first term (on the right hand side) is a rate of convection of rotational energy through the gas by the torques. The second term represents a local rate of loss of mechanical energy to the gas. This ‘lost’ energy must go into internal (heat) energy. The viscous torques therefore cause dissipation within the gas at a rate $G\Omega' dR$ per ring of width dR . Ultimately this energy will be radiated over the upper and lower faces of the disk. We are therefore interested in the dissipation rate per unit plane surface area, $D(R)$. Remembering that each ring has 2 plane faces and thus a plane area $4\pi R dR$, we find

$$D(R) = \frac{1}{2} R^2 v \xi \Omega'^2 \quad (98)$$

6.3 The Accretion Process

In standard non-relativistic accretion theory, it is first assumed that the accreting material has sufficient angular momentum to form a ‘disk’ which is confined closely enough to the orbital plane to be considered a 2D gas flow. This is the ‘thin disk approximation’. The matter moves with maximal angular velocity

$$\Omega = \frac{v_\phi}{R} \leq \sqrt{\frac{GM(R)}{R^3}} \quad (99)$$

The gas is assumed to possess a small radial drift velocity (v_R) in addition to the circular velocity (v_ϕ). v_R is negative near the surface of a central object so that matter is being accreted. The disk is characterised by its surface density $\xi(R, t)$. We now write the mass and angular momentum transport conservation equations.

An annulus of the disk material, lying between R and $R + \Delta R$ has total mass $2\pi R \Delta R \xi$ and total angular momentum $2\pi R^3 \Delta R \xi \Omega$. The rate of change of both of these quantities is given by the net flow from the neighbouring annuli. Again, making the substitution $R_+ = R + \Delta R$ (for clarity), the rate of change of the mass is

$$\begin{aligned} \frac{\partial(2\pi R \Delta R \xi)}{\partial t} &= 2\pi [R v_R(R, t) \xi(R, t) - R_+ v_R(R_+, t) \xi(R_+, t)] \\ &= -2\pi \Delta R \frac{\partial(R v_R \xi)}{\partial R} \end{aligned} \quad (100)$$

In the $R \rightarrow 0$ limit we get

$$R \frac{\partial \xi}{\partial t} + \frac{\partial(R v_R \xi)}{\partial R} = 0 \quad (101)$$

If we take a steady disk structure (i.e. $\frac{\partial}{\partial t} \rightarrow 0$) then (101) can be simplified somewhat to

$$R v_R \xi = \text{constant} \quad (102)$$

As this is an integral of the mass conservation equation, it represents the constant inflow of mass through each point of the disk. We define the accretion rate as

$$\dot{M} = -2\pi R v_R \xi \quad (103)$$

which is constant for all R and has the units of kg/s or often M_\odot/yr . For conservation of momentum, we must include the transport due to the net effects of the viscous torques $G(R, t)$. The rate of change of angular momentum is given by

$$\begin{aligned} \frac{\partial(2\pi R^3 \Delta R \xi \Omega)}{\partial t} &= 2\pi R^3 v_R(R, t) \xi(R, t) \Omega(R) \\ &= -2\pi \Delta R \frac{\partial(R^3 v_R \xi \Omega)}{\partial R} + \frac{\partial G}{\partial R} \Delta R \end{aligned} \quad (104)$$

In the limit $\Delta R \rightarrow 0$ we obtain

$$R \frac{\partial(R^2 \xi \Omega)}{\partial t} + \frac{\partial(R^3 v_R \xi \Omega)}{\partial R} = \frac{1}{2\pi} \frac{\partial G}{\partial R} \quad (105)$$

and for a steady disk

$$R^3 v_R \xi \Omega = \frac{1}{2\pi} (G + C) \quad (106)$$

where C is a constant of integration.

6.3.1 Dissipation Rate for a Black Hole

For the angular velocity (99), we may assume Keplerian motion

$$\Omega = \sqrt{\frac{GM}{R^3}} \quad (107)$$

The angular velocity of the disk material remains Keplerian, increasing inward, until it begins to decrease at a ‘boundary layer’ of radial extent b . Here there exists a radius $R = R_\star + b$, at which $\Omega' = 0$. If $b \ll R_\star$, then Ω is very close to its Keplerian value. Using (95) in (106)

$$R^3 \xi v_R \Omega = R^3 v_R \xi \Omega' + \frac{C}{2\pi} \quad (108)$$

with $R = R_*$, $\Omega' = 0$ and using (103) we have

$$C = -\dot{M}\sqrt{GM R_*} \quad (109)$$

Substituting this back into (108)

$$v_R \xi = \frac{\dot{M}}{3\pi} \left[1 - \sqrt{\frac{R_*}{R}} \right] \quad (110)$$

and using (98) we arrive at

$$D(R) = \frac{3GM\dot{M}}{8\pi R^3} \left[1 - \sqrt{\frac{R_*}{R}} \right] \quad (111)$$

The event horizon of a black hole is at radius

$$R_{schw} = \frac{2GM}{c^2} \quad (112)$$

For $R \gg R_{schw}$ the potential describing the orbits is Keplerian, however, at radii around a few R_{schw} , the effects of general relativity become important and matter is removed from its orbit by instabilities as fast as it arrives. It therefore has very little time to radiate before it disappears. Thus the maximum energy per unit area which can be extracted by this sort of accretion is the specific binding energy of the innermost stable orbit.

This all makes the black hole scenario much easier to study as there is no boundary layer as previously described for accretion onto stars. The boundary condition is that $G(R)$ vanishes at $R_* \sim 3R_{schw}$. So, the dissipation for a black hole can be written, for any R as

$$D(R) = \frac{3GM\dot{M}}{8\pi R^3} \left[1 - \sqrt{\frac{3R_{schw}}{R}} \right] \quad (113)$$

6.3.2 Dissipation Rate for a Fermion Ball

We cannot assume Keplerian motion inside the fermion ball, we must instead use

$$\Omega \leq \sqrt{\frac{GM(R)}{R^3}} = \sqrt{\frac{Gd_\nu}{b_\nu^3}} \sqrt{\frac{\mu(x)}{x^3}} \quad (114)$$

where these are the dimensionless values used in Section 3.3, Equation (64). In (108), we take the point where $\Omega' = 0$ (i.e. maximal Ω) which naturally occurs at the centre of the fermion ball, and this simplifies things greatly. However, we will still keep the formalism to be as general as possible, and consider the case where the maximal Ω_A occurs at a radius R_A . We will later set $R_A = 0$. This gives a solution for C

$$C = 2\pi R_A^3 v_A \xi \Omega_A \quad (115)$$

which gives

$$v_R \xi = \frac{v_R \xi \Omega}{\Omega'} - \frac{R_A^3 v_A \xi \Omega_A}{R^3 \Omega'} \quad (116)$$

Using (103)

$$v \xi = -\frac{\dot{M} \Omega}{2\pi R \Omega'} + \frac{\dot{M} R_A^2 \Omega_A}{2\pi R^3 \Omega'} \quad (117)$$

and inserting into (98) we get

$$\begin{aligned} D(R) &= -\frac{\dot{M}}{4\pi} \left(R \Omega \Omega' - \frac{R_A^2 \Omega_A \Omega'}{R} \right) \\ &= \frac{\dot{M} R \Omega \Omega'}{4\pi} \left[\frac{\Omega_A}{\Omega} \left(\frac{R_A}{R} \right)^2 - 1 \right] \end{aligned} \quad (118)$$

Note that there is no ‘inner radius’ or ‘boundary layer’ for the fermion ball scenario, and thus the gas is deposited in the centre. This makes for an excellent star ‘breeding ground’ at the location of Sgr A*, with an average star birth rate depending upon the mass loss rate \dot{M} .

6.4 Temperature Distribution Due to Accretion

Using the Stefan-Boltzmann law to show the effective temperature from the dissipation rate (assuming instant radiation of the gravitational binding energy)

$$D(R) = \sigma T_{eff}^4(R) \quad (119)$$

6.4.1 Black Hole

The black hole case is trivial. From (113)

$$T_{eff}(R) = \left(\frac{3GM\dot{M}}{8\pi R^3 \sigma} \right)^{\frac{1}{4}} \left[1 - \sqrt{\frac{3R_{schw}}{R}} \right]^{\frac{1}{4}} \quad (120)$$

6.4.2 Fermion Ball

The fermion ball case is, unfortunately, much more tedious. From (118) we arrive at

$$T_{eff}(R) = \frac{\dot{M} G d_\nu}{4\pi \sigma b_\nu^3} x \sqrt{\frac{\mu(x)}{x^3}} \frac{d}{dx} \sqrt{\frac{\mu(x)}{x^3}} \left[\frac{\Omega_A}{\Omega} \left(\frac{x_A}{x} \right)^2 - 1 \right] \quad (121)$$

The reduction of the central part of this equation is documented in Appendix A, which allows us to write the effective temperature distribution as

$$T_{eff}(R) = \left(\frac{\dot{M} G d_\nu}{8\pi \sigma b_\nu^3} \right)^{\frac{1}{4}} \left(\frac{x \mu'(x) - 3\mu(x)}{x^3} \right)^{\frac{1}{4}} \left[\frac{\Omega_A}{\Omega} \left(\frac{R_A}{R} \right)^2 - 1 \right]^{\frac{1}{4}} \quad (122)$$

This may be solved numerically using the mass distribution solution given in Section 3.3, Equations (66) and (67).

6.5 A Toy Model

Although it has been previously mentioned that the gas from the bow-shock is heated to a temperature of $7 \times 10^6 \text{ K}$, the cooling timescale is in the region of 10^5 years. The standard model of accretion was developed in order to explain the accretion of cool gas which has not been shocked by colliding winds. The cold temperature and high density of the accreting gas allows it to settle into an optically thick, geometrically thin disk. Neither of these conditions hold for the centre of the Milky Way. As this is however, a much simpler model to investigate, we make the optically thick, geometrically thin approximation. More complicated Advection Dominated Accretion Flow models have been developed [49, 50], and are much more successful at describing the observed spectrum emanating from the centre of the Milky Way for a black hole scenario.

6.5.1 The Optically Thick Approximation

We make the assumption that the gas is optically thick, so we may treat it as a black body radiator, although Appendix B discusses some of the problems which this approximation may be subject to in the fermion ball scenario. This approximation allows us to calculate the luminosity from the temperature distribution, given by

$$\frac{dL_\nu}{dr} = \frac{16\pi^2 \nu^3 \cos i}{c^2} \frac{r}{e^{\frac{h\nu}{kT}} - 1} \quad (123)$$

As previously mentioned, we take the inclination angle to be 60° and we numerically solve using the boundary condition that $L_\nu(0) = 0$ for the fermion ball. We use data gathered from several different sources and presented in [52].

6.6 Accretion Spectrum

Figure 29 shows the accretion simulation for the fermion ball and black hole scenarios using the mass accretion rate limits imposed by [51]. It is clear that the black hole scenario would produce a large emission in the infra-red to the ultraviolet region $10^{14} \rightarrow 10^{17} \text{ Hz}$, but no emission is detected in that region. As previously mentioned, the lack of emission in the optical and UV regions is due to extinction, and not related to any model. However, this simple model for the accretion onto a black hole does not predict the IR spectrum at all.

Although the fit from the fermion ball scenario is itself far from perfect, Figure 29 clearly shows that the sudden cut-off in the spectrum around

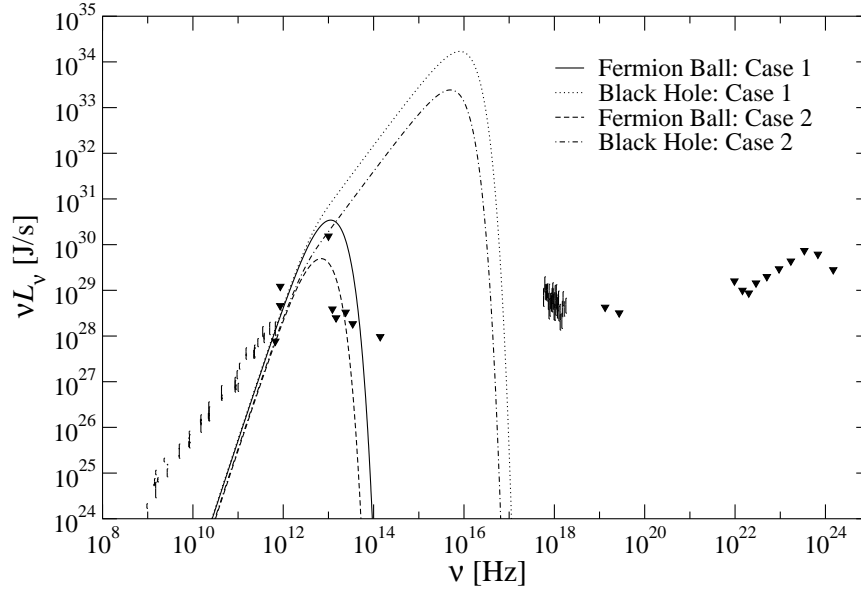


Figure 29: The spectrum of the galactic centre due to accretion of gas. “Case 1” scenarios have $\dot{M}=2.948 \times 10^{-3} M_{\odot}/\text{yr}$ whereas “Case 2” scenarios have $\dot{M}=4.228 \times 10^{-4} M_{\odot}/\text{yr}$. Triangular data points are upper limits.

10^{13}Hz can indeed be explained by an extended source, and this is the phenomenon in which we are concerned. The cut-off is due to shearing forces tending to zero at the centre of the fermion ball. The cut-off can also be explained for the black hole case by using a much lower mass accretion rate. Unfortunately this will have the consequence that luminosities (at frequencies lower than the cut-off value) are too low. Figure 30 displays the spectrum for various mass accretion rates onto a black hole, and Figure 31 the same for the fermion ball scenario.

6.6.1 The Radio and Microwave Spectrum

Although it has been shown that the fermion ball clearly displays the sudden cut-off in the spectrum in the infra-red region, this simple model does not explain the ‘shape’ of the spectrum in the radio and microwave region $10^9 \rightarrow 3 \times 10^{11}\text{Hz}$. Upper limits on the size of the radio source are only a few AU [4], meaning that the emission in this region is not at all due to the overall accretion of matter, but instead is a result of synchrotron radiation (suggested by the polarisation of the detected photons) in some localised process. This is evidence of a central object and poses a serious problem to the fermion ball scenario.

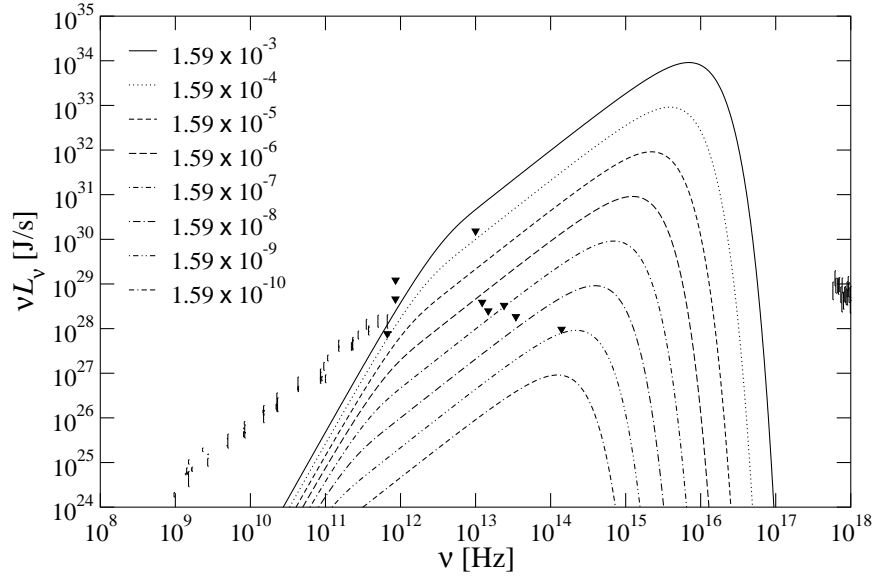


Figure 30: The spectrum of the galactic centre due to accretion of gas onto a black hole. Various mass accretion rates are shown in units of M_\odot/yr .

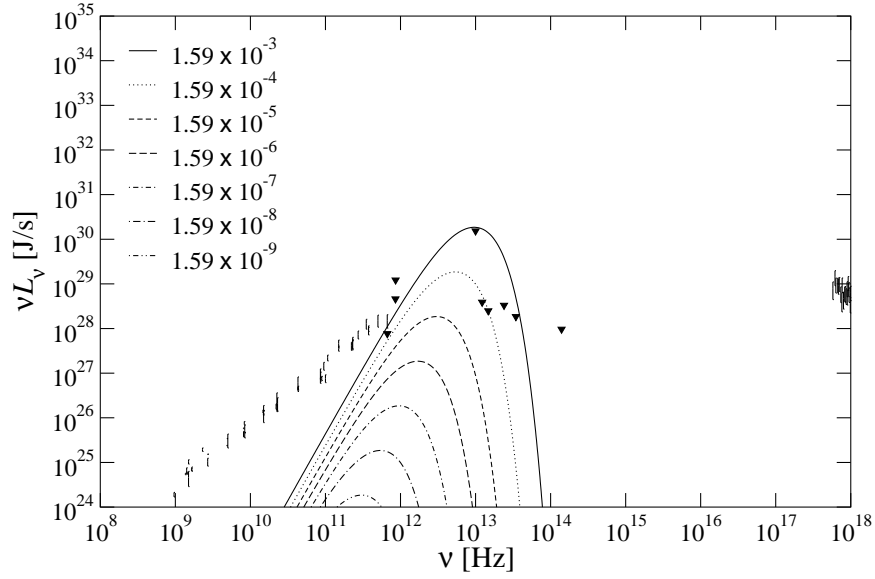


Figure 31: The spectrum of the galactic centre due to accretion of gas onto a fermion ball. Various mass accretion rates are shown in units of M_\odot/yr .

6.6.2 Star Birth

K-band spectra of stars in the Sgr A* cluster [53] reveals that the cluster consists of mainly young, late O \rightarrow early B main sequence stars. The close proximity of the young stars to the galactic centre is an interesting challenge for either star formation theory or dynamical theory as the high temperatures, pressures, velocity dispersions and magnetic field strengths in the central molecular zone inhibit star formation. The black hole scenario is affected even more as there are incredible shearing forces closer to the nucleus. In the fermion ball scenario the potential becomes harmonic at the centre and shearing forces go linearly to zero, practically vanishing at $\sim 0.01\text{pc}$. Using an estimate of new stars simply from the mass accretion rate, a new solar mass star should be expected every 10,000 to 100,000 years in the fermion ball scenario.

7 Fermion Halo and Dark Matter in the Galaxy

*I believe there are
15,747,724,136,275,002,577,605,653,961,181,555,468,044,
717,914,527,116,709,366,231,425,076,185,631,031,296
protons in the universe and the same number of electrons.
– Sir Arthur Eddington*

An extension of the fermion ball theory is to consider fermions with finite temperature [54]. Such an extension results in a fermion halo around the central ball already investigated in this thesis. In this section, we briefly discuss how the finite temperature extension leads to a halo structure and the effect this has upon the dark matter problem in our galaxy [55].

7.1 Dark Matter Within Our Galaxy

It is well known, from the rotation curves of an increasing number of galaxies, that there are substantial amounts of dark matter in the halos of galaxies. Typically, dark matter contributes about 10 times more mass than the ordinary matter which is contained in visible stars, dust and gas. It is worthwhile to speculate that the super-massive compact dark objects at the galactic centres may have something to do with the dark matter in the halos.

In the case of the Milky Way, this dark matter is arranged in a nearly spherically symmetric halo, stretching roughly a third the distance to the Andromeda galaxy in radial component. There are a number of indications from nucleosynthesis [56], micro-lensing [57], structure formation and microwave background data [58], which indicates at least part of this dark matter halo cannot be made of ordinary matter. In the following, we will be primarily concerned with this non-baryonic dark matter which does not interact efficiently with ordinary matter and radiation, except gravitationally.

Cold dark matter scenarios provide an excellent description of the formation of the large-scale structure in the universe. However, they fail on galactic and sub-galactic scales [59] because the absence of velocity dispersion causes the dark matter to sink to the centre. These problems can be bypassed by the introduction of warm dark matter [60], and postulating the existence of a sterile neutrino [25]. The creation of the desired amount of sterile neutrino dark matter in the early universe, with about $\Omega_{\nu_s} = 0.3$ of the critical density today, can be achieved for a sterile neutrino of mass 16keV with a mixing angle θ given by $\sin^2 2\theta \sim 10^{-12}$, see Figure 32. The angle θ describes the mixing of a sterile neutrino with an active neutrino, Equation (1), and therefore makes the dark matter particle observable through its radiative decay into an active neutrino and a photon, with a lifetime of about $\tau \sim 10^{20}$ years. See Figure 33.

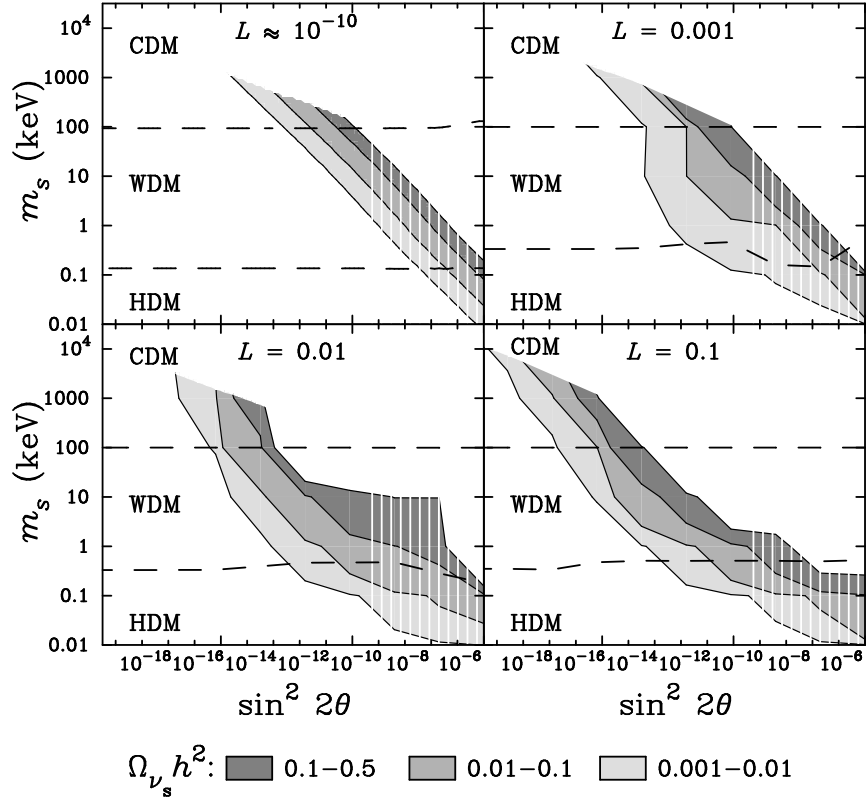


Figure 32: Regions of Ω_{ν_s} produced by resonant and non-resonant electron neutrino mixing with a sterile neutrino. L denotes lepton asymmetry. Regions of parameter space disfavoured by supernova core collapse considerations are shown with vertical stripes. From [25].

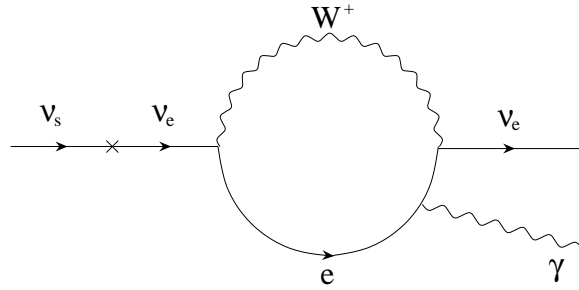


Figure 33: Feynman diagram for the radiative decay of a sterile neutrino into an active neutrino and a photon of energy $\frac{m_{\nu_s}}{2}$.

7.2 The Fermion Halo

It has been shown that a non-relativistic self interacting fermion gas may undergo a first order gravitational phase transition, from a diffuse state to a condensed state [61, 62, 63]. Within a Fermi gas, self energy from gravity is balancing with thermal energy. If the gravity dominates, we have a condensed state, whereas if the thermal energy dominates, we have a diffuse state. The temperature at which the fermions are close to the point of gravitational collapse is called the critical temperature and is where the phase transition occurs. A simple analytical model has been proposed by [64], agreeing quite well with the numerical simulations.

We now briefly discuss the non-relativistic Thomas-Fermi theory for a self gravitating gas of N fermions with mass m_ν at a temperature T enclosed in a sphere of radius R . For large N we can assume the fermions move in a spherically symmetric mean-field potential $\phi(r)$ which satisfies Poisson's equations

$$\frac{d\phi}{dr} = \frac{GN}{r^2} \quad (124)$$

$$\frac{dM(r)}{dr} = 4\pi r^2 m n \quad (125)$$

The number density (n) is determined by the Fermi-Dirac distribution (units $\hbar = c = k = 1$)

$$n = \frac{\rho}{m_\nu} = g_\nu \int \frac{d^3q}{(2\pi)^3} \left[1 + e^{\left(\frac{q^2}{2m_\nu T} + \frac{m_\nu \phi}{T} - \frac{\mu}{T} \right)} \right]^{-1} \quad (126)$$

For each solution $\phi(r)$ of (124), the chemical potential μ is adjusted so that the constraint

$$\int_0^R dr 4\pi r^2 n(r) = N \quad (127)$$

is satisfied. Equations (125) and (126) are integrated using the boundary conditions

$$\phi(0) = \phi_0 \quad M(0) = 0 \quad (128)$$

It is useful to introduce the degeneracy parameter

$$\eta = \frac{\mu}{T} - \frac{m_\nu \phi}{T} \quad (129)$$

with the strongest degeneracy η_0 obtained at the centre, fixed by the condition $M(R) = m_\nu N$, where R is the outer boundary. Outside of R , we have the usual $\propto \frac{1}{r}$ Newtonian potential. Equations (125), (127) and (126) define the gravitational Thomas-Fermi equation, which is solved numerically.

One first solves (125) to yield $M(R)$ as a function of η_0 , leaving 3 free parameters: N , T and R . N is fixed by setting the fermion mass and using

an appropriate total mass consistent with observation. We make the simple calculation $N = \frac{M}{m_\nu}$.

In [55], the values $m_\nu = 15\text{keV}$, $M = 2 \times 10^{12}M_\odot$, $R = 200\text{kpc}$ and $T = 3.75 \times 10^{-3}\text{K}$ were used. The radius limit is based upon the estimated size of the galaxy halo. The temperature is estimated as a result of violent relaxation [65], and is thus directly related to the gravitational plus thermal energy.

The solution is a fermion ball (as investigated in this thesis) alongside a low density halo, extending out to the radius R .

7.3 Rotation Curve of Our Galaxy

Using the numerical mass distribution of the halo, the rotation curve for objects within our galaxy may be calculated. The bulge and disk must also be included for comparison to data. The total rotation curve for our galaxy is shown in Figure 34. The bulge is modelled as a spherically symmetric matter distribution [66] in the form

$$\rho_b(s) = \frac{e^{-hs}}{2s^3} \int_0^\infty du \frac{e^{-hsu}}{[(u+1)^8 - 1]^{\frac{1}{2}}} \quad (130)$$

where $s = \left(\frac{r}{r_0}\right)^{\frac{1}{4}}$, r_0 is the effective radius of the bulge. We adopt values such that $M_b = 1.5 \times 10^{10}M_\odot$ [67]. The contribution of the disk's circular velocity component is modelled as [68]

$$\Theta_d(r)^2 = \Theta_d(r_0)^2 \frac{1.97 \left(\frac{r}{r_0}\right)^{1.22}}{\left[\left(\frac{r}{r_0}\right)^2 + 0.78^2\right]^{1.43}} \quad (131)$$

where we take $r_0 = 13.5\text{kpc}$ and $\Theta_d(r_0) = 100\text{km/s}$. We assume (for simplicity) that the disk does not influence the mass distribution of either the bulge or the halo.

The rotation curve clearly shows that the standard disk and bulge models, in combination with the halo theory, describe reasonably the circular velocity distribution within our galaxy to just beyond a distance of 20kpc. We conclude that the fermion halo sufficiently describes the dark matter distribution within our own galaxy.

In summary, the Thomas-Fermi theory applied to finite temperature, self gravitating, fermionic gas yields a mass distribution explaining the dark matter distribution within the Milky Way halo, whilst also producing a fermion ball at the centre. This theory therefore allows that the fermions in the halo are the same as those at the galactic centre, Sgr A*.

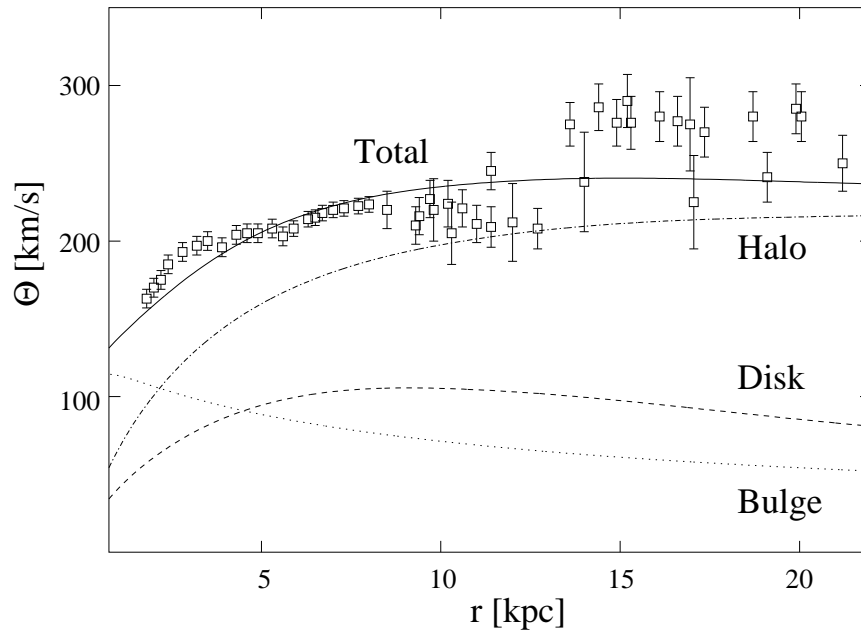


Figure 34: Fit to the Galactic rotation curve. Data points are from [69] and the graph itself is from [55].

8 Conclusions

*The universe is like a safe to which there is a combination,
but the combination is locked up in the safe.
– Peter de Vries*

We have shown that the motion of stars S0-1, S0-2 and S0-4, in the vicinity of the galactic centre, may be fitted by either a black hole or fermion ball scenario, and that these two scenarios have nearly identical χ^2 values. However, further observations should allow discrimination between the two scenarios within a timeframe no longer than 40 years.

The phase space plots of star position and velocity components in our line of sight, reveal distinctive regions which favour a particular scenario. We present the phase space analysis of these parameters as the best technique to discriminate between the two scenarios. A measurement of either z or v_z would dramatically reduce the required observational time to under a decade. A measurement of both parameters could result in instant discrimination.

We have also shown that a simple Newtonian, optically thick, geometrically thin black hole accretion model cannot explain the observed cut-off around 10^{13}Hz in the spectrum of Sgr A*. This model is however, known to be incorrectly implemented in the case of our galactic centre and a more accurate model, such as an Advection Dominated Accretion Flow model would reveal that the black hole scenario does indeed predict the IR cut-off. Following the same modelling technique, a fermion ball scenario explains the cut-off quite adequately and also encourages material to be deposited at the centre, where there are no shear forces. This would be an excellent ‘breeding ground’ for new stars, and therefore could explain the dominance of young stars in that area.

A Reduction of Terms in 6.4.2

Equation (121) contains the problem in x and $\mu(x)$

$$x \sqrt{\frac{\mu(x)}{x^3}} \frac{d}{dx} \sqrt{\frac{\mu(x)}{x^3}}$$

using

$$\begin{aligned} \frac{d}{dx} \left(\frac{u}{v} \right) &= \frac{v\dot{u} - u\dot{v}}{v^2} \\ \frac{d}{dx} (u^n) &= nu^{n-1}\dot{u} \end{aligned}$$

where we assign

$$\begin{aligned} u &= \mu(x)^{\frac{1}{2}} & v &= x^{\frac{3}{2}} \\ \dot{u} &= \frac{1}{2}\mu^{-\frac{1}{2}}\mu'(x) & \dot{v} &= \frac{3}{2}x^{\frac{1}{2}} \end{aligned}$$

it follows that

$$\begin{aligned} \frac{d}{dx} \left(\frac{\mu(x)}{x^3} \right)^{\frac{1}{2}} &= \frac{\sqrt{x} x \mu(x)^{-\frac{1}{2}} \mu'(x) - 3\mu(x)^{\frac{1}{2}}}{2x^3} \\ &\times x \sqrt{\frac{\mu(x)}{x^3}} = \frac{1}{2} \frac{x \mu'(x) - 3\mu(x)}{x^3} \end{aligned}$$

so that we can make the reduction

$$x \sqrt{\frac{\mu(x)}{x^3}} \frac{d}{dx} \sqrt{\frac{\mu(x)}{x^3}} = \frac{1}{2} \frac{x \mu'(x) - 3\mu(x)}{x^3}$$

B Radiation Processes

An (unpolarised) radiation field is defined by the *specific intensity* (I_ν), which gives the flux of energy per second per unit area per solid angle per unit frequency interval

$$dE = I_\nu dA \cos \theta d\nu d\Omega dt$$

The *radiation flux* (F_ν) is the rate at which energy crosses a unit area independent of direction and is obtained by integrating over a solid angle

$$F_\nu = \int I_\nu \cos \theta d\Omega$$

The *specific luminosity* (L_ν) of a source is the flux integrated over an area enclosing the source

$$L_\nu = \int F_\nu dA$$

the variation of I_ν in a medium which is emitting and absorbing is given by the *radiative transfer equation* which simply expresses energy conservation for the radiation field. In the time independent case in a direction \mathbf{n}

$$\mathbf{n} \cdot \nabla I_\nu = -\mu_\nu I_\nu + j_\nu$$

where μ_ν is the absorption coefficient and j_ν the emission coefficient, effectively the properties and state of the medium. It is customary to characterise the medium by the *source function* (S_ν)

$$S_\nu = \frac{j_\nu}{\mu_\nu}$$

The *optical depth* (τ_ν) along a path from source to observer is defined by

$$d\tau_\nu = \mu_\nu ds$$

Giving total specific intensity over an optical depth

$$\frac{dI_\nu}{d\tau_\nu} = -I_\nu + S_\nu$$

If the radiation field corresponds to thermal equilibrium at a temperature T , we know that $I_\nu = B_\nu(T)$, the black body spectrum. Irrespective of the radiation mechanism, we can relate

$$S_\nu = B_\nu(T) = \frac{2h\nu^3}{c^2 \left(e^{\frac{h\nu}{kT}} - 1 \right)}$$

If the medium can be characterised by a temperature T (i.e. thermal emission) then we have Kirchhoff's law, independent of whether the radiation field is Planckian.

$$S_\nu = \frac{j_\nu}{\mu_\nu} = B_\nu(T)$$

In general the source function is determined by the state populations in the medium. A necessary condition for a thermal radiation spectrum is that the optical depth $\tau_\nu \rightarrow \infty$. In this case we say that the medium is *optically thick*, which in general, means that $I_\nu = S_\nu$. On the other hand if $\tau_\nu \rightarrow 0$ we can neglect absorption and we get

$$I_\nu = \int j_\nu ds$$

Such a medium is said to be *optically thin*. Returning to the optically thick case, once we have a source function, we make the following relations (as explained) to give us the observables F_ν or L_ν , depending upon the preference of the experimentalist.

$$\begin{aligned} I_\nu &= S_\nu = \frac{2h\nu^3}{c^2 \left(e^{\frac{h\nu}{kT}} - 1 \right)} \\ F_\nu &= \frac{4\pi h\nu^3 \cos i}{c^2 D^2} \int \frac{R}{e^{\frac{h\nu}{kT}} - 1} dR \\ L_\nu &= 4\pi D^2 F_\nu = \frac{16\pi^2 h\nu^3 \cos i}{c^2} \int \frac{R}{e^{\frac{h\nu}{kT}} - 1} dR \end{aligned}$$

In the text, we have assumed an optically thick medium so that we may simply use a black body as our radiative mechanism. The absorption coefficient is $\mu_\nu \propto \kappa\rho$, which decreases for a low density gas, and thus optical depth decreases. κ is the opacity, and is calculated from the radiative transfer equation

$$\kappa(\nu, T) = \frac{c^2}{8\pi\nu^2} A_{21} \frac{g_2}{g_1} n_1 \left[1 - e^{\frac{h\nu_0}{kT}} \right] \phi(\nu)$$

As temperatures are generally low in the fermion ball case, the gas will not be ionised and therefore κ will also aid in decreasing the optical depth. The gas density is low under both scenarios.

This goes to show that an optically thin approximation may be more appropriate for the fermion ball scenario. In an optically thin accretion disk, a different radiative mechanism must be used as the black body approximation is no longer appropriate, such a valid mechanism could be a thermal bremsstrahlung spectrum.

C Numerical Techniques

The numerical problems in this thesis are Ordinary Differential Equations (ODE's). The first step to solve such a problem is to reduce the system to a series of first order differentials. e.g. for the Lané-Emden Equation (13)

$$\frac{d^2v(x)}{dx^2} = -\frac{v(x)^{\frac{3}{2}}}{x^{\frac{1}{2}}}$$

we may write as two, first order equations

$$z = \frac{dv}{dx} \quad \frac{dz}{dx} = -\frac{v^{\frac{3}{2}}}{x^{\frac{1}{2}}}$$

The simplest way to solve such an equation is to use Euler's method (f is the known derivative of a function, with specified parameters)

$$b_{n+1} = b_n + hf(a_n, b_n)$$

which advances a solution from a_n to $a_{n+1} \equiv a_n + h$. It advances the solution through an interval h , but uses derivative information only at the beginning of that interval, meaning the error is only one power of h lower than the correction $O(h^2)$. e.g. In the Lané-Emden example, if we solve with a numerical step size of 10^{-2} , then the error in each value will be $(10^{-2})^2 = 10^{-4}$ of the correction, which is rather high. Small step sizes must be used for accuracy, but this results in incredibly long run times of programs.

Another technique is the Runge-Kutta method, which takes a 'trial' step to the midpoint of the interval, then uses the value of both a and b at that midpoint to compute a more accurate step across the whole interval.

$$\begin{aligned} k_1 &= hf(a_n, b_n) \\ k_2 &= hf\left(a_n + \frac{1}{2}h, b_n + \frac{1}{2}k_1\right) \\ b_{n+1} &= b_n + k_2 + O(h^3) \end{aligned}$$

This is a third order Runge-Kutta as the error is of that order. In this thesis, a fourth order Runge-Kutta was employed in mass distribution solutions, with a step size of 10^{-6} , giving an error of 10^{-24} times the correction for each step.

All code was written in C and is available¹ under the GNU Public Licence, requiring the GNU Science Library² for compilation.

¹<http://neutrino.phy.uct.ac.za>

²<http://sources.redhat.com/gsl>

References

- [1] L. C. Ho, J. Kormendy, *astro-ph/0003267*; *astro-ph/0003268*
- [2] F. Macchetto, A. Marconi, D. J. Axon, A. Capetti, W. Sparks, P. Crane, *ApJ* **489** (1997) 579
- [3] A. M. Ghez, B. L. Klein, M. Morris, E. E. Becklin, *ApJ* **509** (1998) 678
- [4] D. C. Backer, R. A. Sramek, *ApJ* **524** (1999) 805
- [5] G. C. Bower, D. C. Backer, *ApJL* **496** (1998) 97
- [6] W. Kundt, *ApJSS* **172** (1990) 109
- [7] T. N. Larosa, N. E. Kassim, T. J. Lazio, S. D. Hyman, *AJ* **119** (2000) 207
- [8] F. K. Baganoff *et al.*, *astro-ph/0102151*
- [9] E. Maoz, *ApJL* **494** (1998) 181
- [10] G. Burbidge, F. Hoyle, *ASP Conf. Ser.* **102** The Galactic Center
- [11] R. D. Viollier, D. Trautmann, G. B. Tupper, *Phys. Lett. B* **306** (1993) 79
- [12] N. Bilić, D. Tsiklauri, R. D. Viollier, *Prog. Part. Nucl. Phys.* **40** (1998) 17
- [13] D. Tsiklauri, R. D. Viollier, *Astropart. Phys.* **12** (1999) 199
- [14] R. D. Viollier, *Prog. Part. Nucl. Phys.* **32** (1994) 51
- [15] N. Bilić, F. Munyaneza, R. D. Viollier, *Phys. Rev. D* **59** (1998) 024003
- [16] F. Munyaneza, D. Tsiklauri, R. D. Viollier, *ApJ* **526** (1999) 744
F. Munyaneza, R. D. Viollier, *ApJ* **564** (2002) 274
- [17] D. F. Torres, S. Capozziello, G. Lambiase, *Phys. Rev. D* **62** (2000) 104012
- [18] M. A. Markov, *Phys. Lett.* **10** (1964) 122
- [19] J. Bonn *et al.*, *Nucl. Phys. B* **91** (2001) 273
- [20] Y. Fukuda *et al.* (Super-Kamiokande Collaboration), *Phys. Rev. Lett.* **81** (1998) 1562
- [21] D. E. Groom *et al.*, *Eur. Phys. J. C* **15** (2000) 1

- [22] V. S. Berezinsky, A. V. Gurevich, K. P. Zybin, *Phys. Lett. B* **294** (1992) 221
- [23] E. W. Kolb, M. S. Turner, *The Early Universe*, Addison-Wesley (1989)
- [24] X. Shi, G. M. Fuller, *Phys. Rev. Lett.* **82** (1999) 2832
- [25] K. Abazajian, G. M. Fuller, M. Patel *Phys. Rev. D* **64** (2001) 023501
- [26] D. H. Lyth, *Phys. Lett. B* **488** (2000) 417
- [27] K. Tamvakis, D. Wyler, *Phys. Lett. B* **112** (1982) 451
- [28] T. Goto, M. Yamaguchi, *Phys. Lett. B* **276** (1992) 103
- [29] L. Covi, H. B. Kim, J. E. Kim, L. Roszkowski, *J. High Energy Phys.* **0105** (2001) 033
- [30] G. M. Fuller, R. A. Malaney, *Phys. Rev. D* **43** (1991) 3136
- [31] E. W. Kolb, M. S. Turner, *Phys. Rev. Lett.* **67** (1991) 5
- [32] S. Dodelson, L. M. Widrow, *Phys. Rev. Lett.* **72** (1994) 17
- [33] S. Sarkar, *Rep. Prog. Phys.* **59** (1996) 1493
- [34] D. H. Lyth, D. Roberts, M. Smith, *Phys. Rev. D* **57** (1998) 7120
- [35] N. Bilić, R. Lindebaum, G. B. Tupper, R. D. Viollier, *Phys. Lett. B* **515** (2001) 105
- [36] M. Colpi, S. Shapiro, I. Wasserman, *Phys. Rev. Lett.* **57** (1986) 20
- [37] A. S. Parkins, D. F. Walls, *Phys. Rep.* **303** (1998) 1
- [38] A. M. Ghez, M. Morris, E. E. Becklin, A. Tanner, T. Kremenek, *Nature* **407** (2000) 349
- [39] A. Eckart, R. Genzel, T. Ott, R. Schödel, *MNRAS* **331** (2002) 917
- [40] L. H. Thomas, *Proc. Cambridge Phil. Soc.* **23** (1924) 542
E. Fermi, *Zeit. Phys.* **48** (1928) 73
- [41] S. Esposito, *physics/0111167*
- [42] R. C. Tolman, *Phys. Rev.* **55** (1939) 364
- [43] R. C. Tolman, *Relativity, Thermodynamics and Cosmology*, Oxford (1934)
- [44] J. R. Oppenheimer, G. M. Volkoff, *Phys. Rev.* **55** (1939) 374

- [45] S. Chandrasekhar, *Stellar Structure*, University of Chicago Press (1939)
- [46] F. Melia, H. Falcke, *Annu. Rev. Astron. Astrophys.* **39** (2001) 309
- [47] J. Frank, A. King, D. Raine, *Accretion Power in Astrophysics*, Cambridge (1992)
- [48] F. Yusef-Zadeh, M. Morris, *ApJL* **371** (1991) 59
- [49] M. J. Rees, *In the Galactic Centre*, New York:AIP (1982)
- [50] Narayan *et al*, *ApJ* **492** (1998) 554
- [51] F. Melia, *ApJL* **387** (1992) 25
- [52] R. Coker, *PhD Thesis*, University of Arizona (1999)
- [53] S. Gezari, A. M. Ghez, E. E. Becklin, J. Larkin, I. S. McLean, M. Morris, *astro-ph/0205186*
- [54] N. Bilić, R. D. Viollier, *Phys. Lett. B* **408** (1997) 75
- [55] N. Bilić, G. B. Tupper, R. D. Viollier, *astro-ph/0111366*
- [56] H. Kurki-Suonio, E. Sihvola, *Phys. Rev. D* **63** (2001) 083508
- [57] K. Griest, *et al.* *astro-ph/9506016*
- [58] X. Chen, S. Hannestad, R. J. Scherrer, *Phys. Rev. D* **65** (2002) 123515
- [59] A. Tasitsiomi, *astro-ph/0205464*
- [60] Y. P. Jing, *Mod. Phys. Lett. A* **16** (2001) 1795
- [61] N. Bilić, R. D. Viollier, *Phys. Lett. B* **408** (1997) 75
- [62] N. Bilić, R. D. Viollier, *Gen. Rel. Grav.* **31** (1999) 1105
- [63] N. Bilić, R. D. Viollier, *Eur. Phys. J. C* **11** (1999) 173
- [64] P-H. Chavanis, *Phys. Rev. E* **65** (2002) 056123
- [65] D. Lynden-Bell, *MNRAS* **136** (1967) 101
- [66] G. de Vaucouleurs, W. D. Pence, *ApJ* **83** (1978) 1163
- [67] P. D. Sackett, *ApJ* **483** (1997) 103
- [68] M. Persic, P. Salucci, F. Stell, *MNRAS* **281** (1986) 27
- [69] R. P. Olling, M. R. Merrifield, *MNRAS* **311** (2000) 361

Acknowledgements

Firstly I would like to thank my supervisor, Prof. R. D. Viollier, for this interesting topic and the funding I needed to survive. Thanks go to Dr. G. Tupper for help on the Newtonian derivations and to Prof. A. Ghez, Dr. F. Baganoff and Dr. R. Coker for their communal spirit in the sharing of their data. Physics needs more people with your attitude, in my opinion ‘read it from the graph!’ is a line spoken by frauds and ASCII is always welcome!

I must thank the UCT funding and housing departments for much amusement they have given me in their amazing ability to be incompetent in every way possible. My thanks for zero funding and an overpriced shanty.

Credit must be given to the GNU community, whom collectively have created an operating system which has allowed me to run the simulations and produce in a professional manner, this thesis and the figures therein. Thanks to Wayne Kerr for many enlightening discussions on the numerics.

Thanks to the entire staff of the UCT physics department, you made me feel very welcome! I would also like to thank the great friends I have made in the time I have spent in this beautiful country. Hopefully we can all have a pint on my turf next time!

I am very grateful to my parents, without their support this adventure would not have been possible. Same goes for the big man upstairs, who is always looking out for me.